

# Contributions from lithospheric and upper-mantle heterogeneities to upper crustal seismicity in the Korean Peninsula

Sungho Lee<sup>1</sup>, Arushi Saxena<sup>2,3</sup>, Jung-Hun Song<sup>1</sup>, Junkee Rhie<sup>1</sup> and Eunseo Choi<sup>2</sup>

<sup>1</sup>School of Earth and Environmental Sciences, Seoul National University, 1 Gwanak-ro, Gwanak-gu, Seoul 08826, Republic of Korea. E-mail: [rhie@snu.ac.kr](mailto:rhie@snu.ac.kr)

<sup>2</sup>Center for Earthquake Research and Information, University of Memphis, 3890 Central Ave., Memphis, TN 38152, USA

<sup>3</sup>Department of Geological Sciences, University of Florida, 241 Williamson Hall, Gainesville, FL 32611, USA

Accepted 2021 December 22. Received 2021 December 21; in original form 2021 August 12

## SUMMARY

The Korean Peninsula (KP), located along the eastern margin of the Eurasian and Amurian plates, has experienced continual earthquakes from small to moderate magnitudes. Various models to explain these earthquakes have been proposed, but the origins of the stress responsible for this region's seismicity remain unclear and debated. This study aims to understand the stress field of this region in terms of the contributions from crustal and upper-mantle heterogeneities imaged via seismic tomography using a series of numerical simulations. A crustal seismic velocity model can determine the crustal thickness and density. Upper-mantle seismic velocity anomalies from a regional tomography model were converted to a temperature field, which can determine the structures (e.g. lithospheric thickness, subducting slabs, their gaps, and stagnant features) and density. The heterogeneities in the crustal and upper mantle governed the buoyancy forces and rheology in our models. The modelled surface topography, mantle flow stress, and orientation of maximum horizontal stress, derived from the variations in the crustal thickness, suggest that model with the lithospheric and upper-mantle heterogeneities is required to improve these modelled quantities. The model with upper-mantle thermal anomalies and east–west compression of approximately 50 MPa developed a stress field consistent with the observed seismicity in the KP. However, the modelled and observed orientations of the maximum horizontal stress agree in the western KP but they are inconsistent in the eastern KP. Our analysis, based on the modelled quantities, suggested that compressional stress and mantle heterogeneities may mainly control the seismicity in the western area. In contrast, we found a clear correlation of the relatively thin lithosphere and strong upper-mantle upwelling with the observed seismicity in the Eastern KP, but it is unclear whether stress, driven by these heterogeneities, directly affects the seismicity of the upper crust.

**Key words:** Numerical modelling; Seismic tomography; Dynamics: seismotectonics; Intraplate processes; Rheology: crust and lithosphere; Rheology: mantle.

## 1. INTRODUCTION

The Korean Peninsula (KP) is located along the eastern margin of the Eurasian and Amurian plates. Although it is located far from active tectonic boundaries (Fig. 1a), it has experienced moderate-sized earthquakes, which have resulted in significant structural damage and numerous fatalities (Houng & Hong 2013). According to instrument-recorded activity since 1978, the largest earthquake was the Gyeongju earthquake ( $M_L$  5.8), which occurred in Gyeongju on the southeastern KP on 12 September 2016 (Kim *et al.* 2016; Fig. 1b). The ground shaking generated by this earthquake was felt throughout the country, and the earthquake was followed by numer-

ous aftershocks (Woo *et al.* 2019). The occurrence of the Gyeongju earthquake surprised the inhabitants of South Korea, as the KP is generally considered a stable tectonic region with a low seismic hazard (Kim *et al.* 2016).

The origin of KP seismicity is obscure because the KP shows low and distributed geodetic strain rates on the order of  $10^{-9}$  yr<sup>-1</sup> (Jin *et al.* 2006) and a negligible association with known tectonic fabrics and crustal thickness variations, as observed in previous studies (Figs 1b and c). According to Lee & Yang (2006), seismicity in the KP exhibits a diffuse seismic zone lacking a concentration of earthquakes, along with weaknesses such as surface lineaments, which dominantly show an NNE direction (Fig. 1b). Noting the continent-

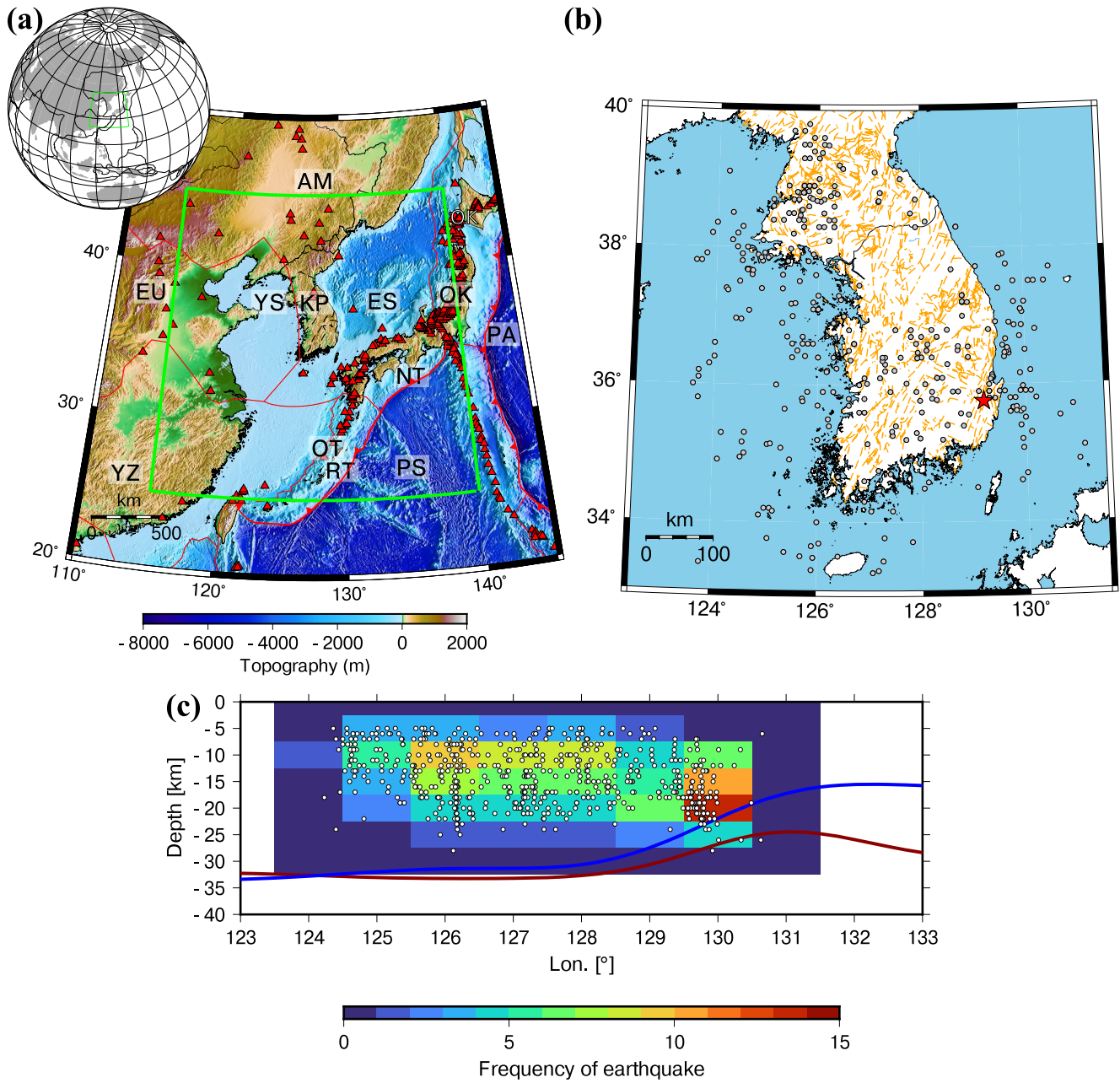


**Figure 1.** (a) Map of Northeast Asia. Solid red lines denote plate boundaries while red saw-toothed lines indicate convergent plate boundaries (Bird 2003). The green solid box indicates the numerical model. Red triangles indicate Cenozoic volcanism (Global Volcanism Program 2013). AM: Amurian Plate; ES: East Sea (Sea of Japan); EU: Eurasian Plate; KP: Korean Peninsula; NT: Nankai Trough; OK: Okhotsk Plate; PA: Pacific Plate; PS: Philippine Sea Plate; RT: Ryukyu Trench; YS: Yellow Sea; and YZ: Yangtze Plate. (b) Earthquake epicentres from the Korea Meteorological Administration (KMA) catalogue between 1978 and 2020. Grey circles and a red star respectively indicate the  $M_L \geq 3$  events and Gyeongju earthquake ( $M_L$  5.8). Orange lines indicate surface lineaments. (c) Depth distribution of the hypocentres and the earthquake frequency ( $M_L \geq 3$ ) across an area of  $1.0^\circ \times 5\text{ km}$ . Dark red and blue lines indicate the moho depth (Mohorovičić discontinuity) along  $36^\circ\text{N}$  and  $38^\circ\text{N}$ , respectively.

to-ocean transition (COT) across the eastern margin of the KP, Soh *et al.* (2018) utilized numerical models to show that the maximum horizontal stress is eastwards, as accumulated by the lateral discontinuity in the elastic moduli at the COT. However, there is a lack of distinct evidence for a trend of eastwards increasing seismicity (Fig. 1c). Moreover, the earthquake frequency near  $126^\circ\text{E}$  is high even with the weak variations in the crustal thickness (Fig. 1c), implying that we do not understand the contribution from varying crustal thicknesses to this region's seismicity. Lee & Yang (2006)

speculated that the diffuse seismicity may be a response to the lithosphere modified by Mesozoic orogenies (e.g. Park *et al.* 2018), thus altering the regional stress field.

The stress field can be significantly influenced by lateral variations in the mantle (e.g. Lithgow-Bertelloni & Guynn 2004). Recent seismic tomographic models consistently show sharp and strong lateral variations in the upper-mantle velocities beneath the KP (Tao *et al.* 2018; Song *et al.* 2020). Tao *et al.* (2018) imaged the upper-mantle structures beneath northeast Asia (NE Asia) with a

full-waveform inversion tomography model. Images at depths of 100 and 200 km show the variation from a relatively high-velocity S-wave structure in the Yellow Sea (YS) to a low-velocity structure in the East Sea (ES, Fig. 2a and b). These characteristics are consistent with other images resolved by Song *et al.* (2020). They imaged the upper-mantle structures beneath the southern Korean Peninsula (SKP) using teleseismic relative arrival time data from dense local seismic arrays. Sharp and strong lateral variations in the upper-mantle velocities ( $dV_p$  of  $-4.23$  to  $3.46$  per cent;  $dVs$  of  $-5.87$  to  $5.13$  per cent) were observed beneath the SKP, which were interpreted as a contrast between the cold thick cratonic lithosphere root in the southwestern SKP and the modified thin continental margin lithosphere. Although the lithospheric and upper-mantle heterogeneities are known to have significant effects on crustal seismicity (e.g. Craig *et al.* 2011; Mazzotti 2007; Sloan *et al.* 2011; Mooney *et al.* 2012; Saxena *et al.* 2021), no studies have considered the heterogeneous lithosphere and upper mantle to understand the seismicity of the KP.

This study investigates the contributions from the lithospheric structures and upper-mantle heterogeneities with respect to the seismicity of the KP using numerical models. Geodynamic numerical modelling is useful for linking stress sources to crustal seismicity owing to its capability of computing stress fields based on one or more selected contributing factors, such as lithospheric structures and mantle heterogeneities. For instance, this capability enabled Saxena *et al.* (2021) to find a reasonable correlation among the foundering lithospheric root, as revealed by seismic tomography, the modelled quantities, including the stress field and seismicity in the central and eastern United States (CEUS), and a region analogous to the KP, in terms of the large distance from the plate boundaries and low tectonic strain rates. Following the modelling procedure applied to the CEUS by Saxena *et al.* (2021), we inverted the regional tomography reported in Tao *et al.* (2018) to obtain a temperature field to determine the density and viscosity of the assumed compositions. Far-field tectonic stresses and crustal thickness were also considered.

In the following sections, we first introduce the procedure used to invert the seismic velocity anomalies into those of temperature under geochemical constraints, and then describe how the numerical models were constructed (Section 2). Then, the model results are presented in terms of the spatial distributions of the modelled quantities (i.e. velocity, viscosity, temperature, surface topography and mantle flow stress), a statistical analysis, and orientation of the maximum horizontal stress (Section 3). Next, we discuss the results by comparing the model predictions with geophysical observations (Section 4). Finally, we address the contribution from the heterogeneous lithosphere and mantle to the upper crustal seismicity in the KP.

## 2. MODELLING METHOD

### 2.1. Inverting seismic velocity for temperature

A key step in inverting velocity anomalies in a seismic tomography model for temperature is to determine the derivatives of the  $P$ - and  $S$ -wave velocities (i.e.  $V_p$  and  $V_s$ , respectively) with respect to the temperature ( $T$ ). Following Goes *et al.* (2000), we expressed the velocity derivative ( $\partial V/\partial T$ ) as the sum of the anharmonic (anh) and anelastic (ane) terms:

$$\frac{\partial V}{\partial T} = \left( \frac{\partial V}{\partial T} \right)_{\text{anh}} + \left( \frac{\partial V}{\partial T} \right)_{\text{ane}} . \quad (1)$$

Following Goes *et al.* (2000), we obtained  $(\partial V/\partial T)$  for the  $P$  and  $S$  waves as follows:

$$\begin{aligned} \frac{\partial V_p}{\partial T} &= \frac{1}{2\sqrt{\rho}} \frac{1}{\sqrt{K + \frac{4}{3}G}} \frac{\partial (K + \frac{4}{3}G)}{\partial T} - \frac{\sqrt{K + \frac{4}{3}G}}{2\rho^{1.5}} \frac{\partial \rho}{\partial T} \\ &\quad + Q_p^{-1} \frac{aE}{2RT^2 \tan \frac{\pi a}{2}} \end{aligned} \quad (2)$$

$$\frac{\partial Vs}{\partial T} = \frac{1}{2\sqrt{\rho}} \frac{1}{\sqrt{G}} \frac{\partial G}{\partial T} - \frac{\sqrt{G}}{2\rho^{1.5}} \frac{\partial \rho}{\partial T} + Q_s^{-1} \frac{aE}{2RT^2 \tan \frac{\pi a}{2}}, \quad (3)$$

where  $K$  and  $G$  are the bulk and shear moduli, respectively,  $\rho$  is the mass density,  $Q_p$  and  $Q_s$  are the quality factors for the  $P$  and  $S$  waves, respectively,  $a$  is an exponent describing the frequency dependence of the attenuation,  $E$  is the activation energy and  $R$  is the gas constant. On the right-hand sides of eqs (2) and (3), the first and second terms are relevant to the anharmonicity while the other is relevant to the anelasticity. Appendix A presents the derivation of the partial derivatives on the right-hand side of eqs (2) and (3). Again, following Goes *et al.* (2000), we used the following forms of the quality factors:

$$Q_p^{-1} = \left( 1 - \frac{4}{3} \left( \frac{Vs}{V_p} \right)^2 \right) Q_k^{-1} + \frac{4}{3} \left( \frac{Vs}{V_p} \right)^2 \left( A\omega^a \exp \left( \frac{a(E + PV)}{RT} \right) \right)^{-1} \quad (4)$$

$$Q_s^{-1} = \left( A\omega^a \exp \left( \frac{a(E + PV)}{RT} \right) \right)^{-1}, \quad (5)$$

where  $Q_k$  is the bulk attenuation constant,  $A$  is the scaling factor,  $\omega$  is the seismic frequency,  $P$  is the pressure and  $V$  is the activation volume.

The anharmonic terms in eqs (2) and (3) were evaluated based on the mineral composition of the mantle xenoliths found in the KP while the anelastic term was evaluated with parameters for olivine, a major constituent mineral of the upper mantle. Peridotite xenoliths hosted by alkali basalts are lherzolite and magnesian harzburgite (Choi 2012). The constituent minerals include forsterite-rich olivine (Oliv), enstatite-rich orthopyroxene (Opx), diopside-rich clinopyroxene (Cpx) and spinel (Spi). The modal proportions of peridotite show that Oliv is 40–83 per cent, Opx is 14–32 per cent, Cpx is 2–23 per cent and Spi is 0.4–6 per cent (Choi 2012). Based on these data, we selected the average compositions of lherzolite and harzburgite for upper-mantle rocks, which are composed of four minerals (i.e. Oliv, Opx, Cpx and Spi): Lherzolite (Oliv: 62 per cent, Opx: 24 per cent, Cpx: 12 per cent and Spi: 2 per cent) and harzburgite (Oliv: 81.0 per cent, Opx: 14 per cent, Cpx: 2 per cent and Spi: 3 per cent, McDonough & Rudnick 1998). Table S1 lists the elastic parameters of the minerals. The anelastic parameters for olivine are as follows:  $A = 1.48 \times 10^{-1}$ ,  $E = 500 \times 10^3 \text{ J mol}^{-1}$ ,  $V = 20 \times 10^{-6} \text{ m}^3 \text{ mol}^{-1}$ ,  $a = 0.15$ ,  $R = 8.314 \text{ J k}^{-1} \text{ mol}^{-1}$  and  $\omega = 1 \text{ Hz}$  (Goes *et al.* 2000).

The Newton–Raphson method was applied to  $R = \partial V_{\text{anh}} + \partial V_{\text{ane}} - \partial V_{\text{obs}}$  to find temperature anomalies that minimize the residual  $R$ . In this study, we only inverted the perturbation of the  $S$ -wave velocity because it is more sensitive to temperature than the  $P$ -wave velocity (Priestley & McKenzie 2006). The obtained temperature anomalies were added to an averaged geotherm of the continental and oceanic upper mantle (Fig. S1; Turcotte & Schubert 2002). The final temperature field was used as input for the numerical models described later.

Our numerical models used the temperature field inverted from the regional tomographic model of Tao *et al.* (2018) to consider the

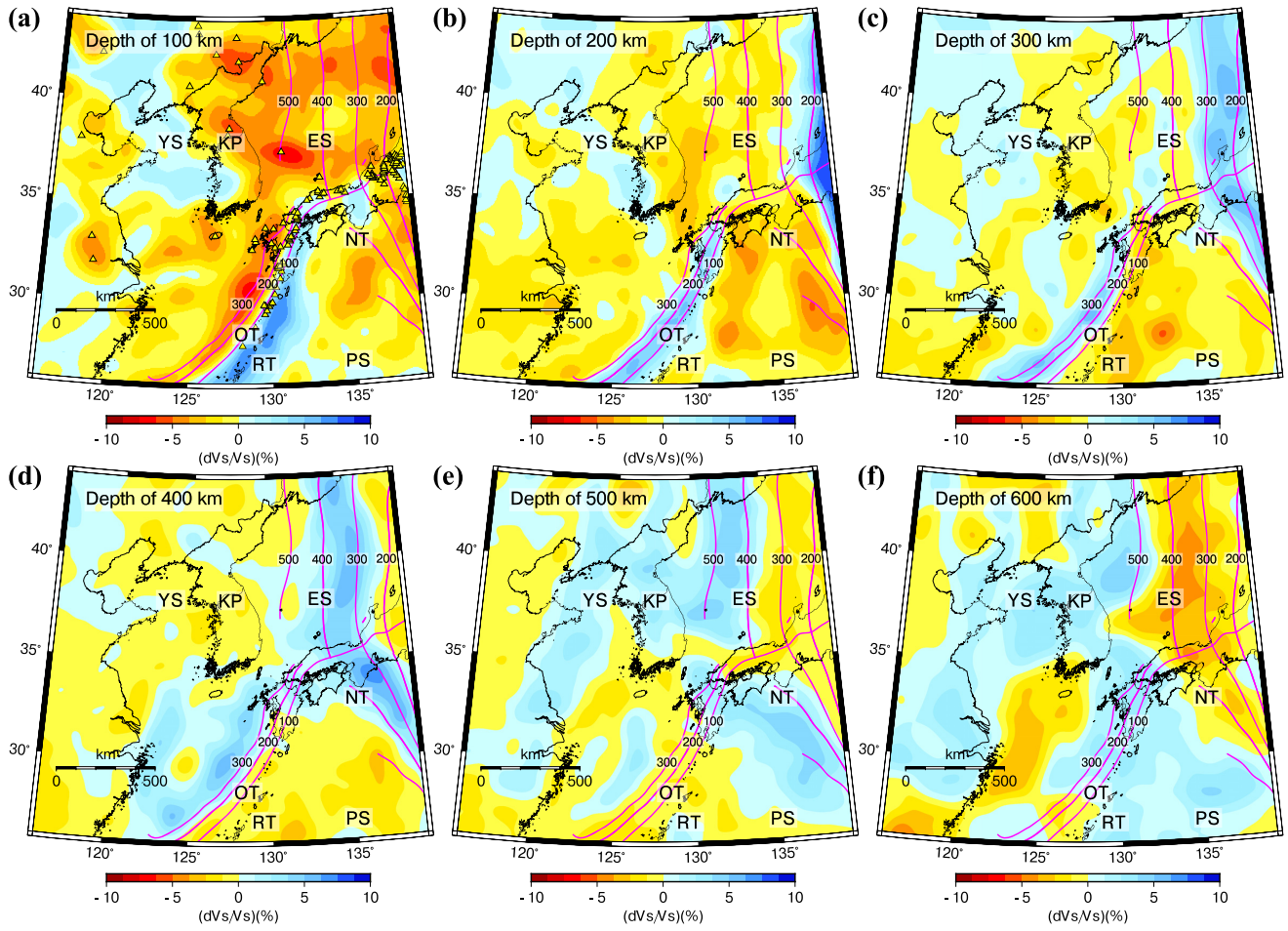


**Figure 2.** *S*-wave anomalies from Tao *et al.* (2018) at depths of (a) 100, (b) 200, (c) 300, (d) 400, (e) 500 and (f) 600 km. The depths of the subducting oceanic slabs are indicated by solid magenta contours at 100-km intervals based on the Slab2.0 model (Hayes *et al.* 2018). Yellow triangles in (a) indicate Cenozoic volcanism (Global Volcanism Program 2013). Refer to Fig. 1(a) for abbreviation definitions.

heterogeneous lithosphere and upper mantle. This model had a spatial extent of 90°–150°E, 10°–60°N and 0–800 km, and a resolution of 0.25° × 0.25° × 10 km. The tomography showed subducting slabs, where the slab geometry is consistent with Slab2.0 (Hayes *et al.* 2018). We conducted temperature inversion for a smaller domain focusing on the KP and its surroundings [115°–140°E and 25°–45°N (green box in Fig. 1a) and 0–660 km] using the Voigt average isotropic *S*-wave speed,  $\sqrt{\frac{V_{SV}^2 + 2V_{SH}^2}{3}}$  (Figs 2 and 3). To promote the reproducibility of our study, we have made the inversion script available online (Lee *et al.* 2020). The script was implemented into the Python programming language and stored as a Jupyter Notebook.

## 2.2. Numerical modelling

### 2.2.1 Governing equations and modelling software

We created a series of numerical models using ASPECT Version 2.2.0 (Kronbichler *et al.* 2012; Glerum *et al.* 2017; Heister *et al.* 2017; Rose *et al.* 2017; Fraters *et al.* 2019; Bangerth *et al.* 2020; Heister *et al.* 2020), which is an open-source finite element code; we used it to model lithospheric deformation and thermochemical

convection in the mantle. We chose the following set of governing equations under the Boussinesq approximation:

$$-\nabla \cdot \tau(u) + \nabla P = \rho g, \quad (6)$$

$$-\nabla \cdot u = 0, \quad (7)$$

$$\rho C_p \left( \frac{\partial T}{\partial t} + u \cdot \nabla T \right) = k \nabla^2 T, \quad (8)$$

$$\frac{\partial C_i}{\partial t} + u \cdot \nabla C_i = q_i, \quad (9)$$

where  $\tau(u)$  is the deviatoric stress tensor (Pa),  $u$  is the velocity vector ( $\text{m s}^{-1}$ ),  $P$  is pressure (Pa),  $\rho$  is density ( $\text{kg m}^{-3}$ ),  $g$  is the gravity vector ( $\text{m s}^{-2}$ ),  $C_p$  is heat capacity ( $\text{J kg}^{-1}\text{K}^{-1}$ ),  $T$  is temperature (K),  $t$  is time (s),  $k$  is heat conductivity ( $\text{W m}^{-1}\text{K}^{-1}$ ),  $C_i$  is the composition,  $q_i$  is the compositional source term,  $\tau$  is the deviatoric stress tensor, defined as  $\tau(u) = 2\eta(\epsilon(u) - \frac{1}{3}(\nabla \cdot u)I)$ ,  $\epsilon$  is the strain rate tensor, given as  $\epsilon(u) = \frac{1}{2}(\nabla u + (\nabla u)^T)$  and  $\eta$  is the viscosity (Pa·s). Eqs (6)–(9) describe the linear momentum balance, continuity, advection-diffusion of heat energy, and advection of the composition field. We did not consider heat production processes, such as shear heating and heat production, due to radioactive decay. Heat capacity and conductivity were assumed to be constant. Diffusion and dislocation creep, with plastic yield, were assumed

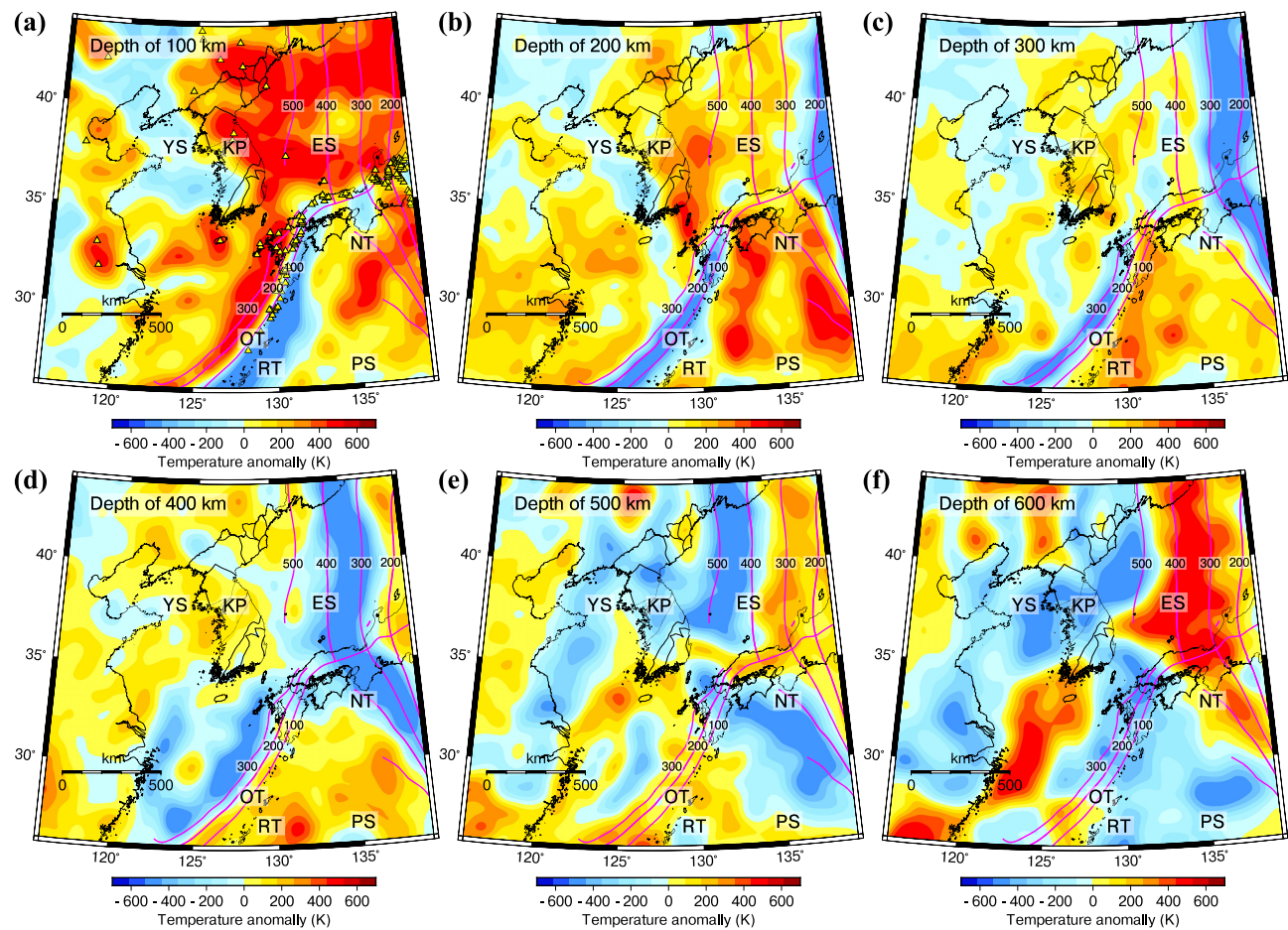


**Figure 3.** Inverted temperature anomalies at depths of (a) 100, (b) 200, (c) 300, (d) 400, (e) 500 and (f) 600 km. The depths of the subducting oceanic slabs are indicated by solid magenta contours at 100-km intervals based on the Slab2.0 model (Hayes *et al.* 2018). Yellow triangles in (a) indicate Cenozoic volcanism (Global Volcanism Program 2013). Refer to Fig. 1(a) for abbreviation definitions.

such that an effective viscosity was determined as a harmonic average of the viscosities resulting from the two creeping mechanisms and plastic yield. Glerum *et al.* (2017) provide more details on the formulations of the viscoplasticity in ASPECT.

#### 2.2.2 Numerical model setup

The model domain was defined as a spherical cap with dimensions of  $115^{\circ}$ – $140^{\circ}$ E,  $25^{\circ}$ – $45^{\circ}$ N and 0–660 km (Fig. 4a). It was discretized into  $0.25^{\circ} \times 0.25^{\circ} \times 10$  km for the entire numerical domain, but the elements within the top 50 km were further refined to  $0.125^{\circ} \times 0.125^{\circ} \times 5$  km such that the crustal thickness variation was adequately resolved (Fig. 4a).

The domain was composed of three layers: upper crust, lower crust and mantle. The upper and lower crustal thicknesses and densities were obtained from the CRUST1.0 model (Laske *et al.* 2013; Fig. 5). The upper crustal density was  $2608 \text{ kg m}^{-3}$ , consisting of the thickness-weighted average of water, sediment, and upper crust. The lower crust in our models, corresponding to the middle and lower crust of CRUST1.0, had a thickness-weighted average density of  $2915 \text{ kg m}^{-3}$ . The rheological parameters and equation of state for the different lithologies considered in our model were based on previous studies (Table 1). Specifically, for the upper crust, lower crust and mantle we used laboratory-derived viscous flow laws of the assumed predominant mineral phase (wet quartzite, wet anorthite

and dry olivine, respectively). This study used a volumetric thermal expansivity ( $\alpha$ ) of  $3 \times 10^{-5} \text{ K}^{-1}$  for mantle (Turcotte & Schubert 2002), but a value of zero for the crust (Table 1). We modelled two buoyancy effects driven by the crust and mantle. One is associated with the crustal thickness, as defined by CRUST1.0 (Laske *et al.* 2013). We then imposed a zero value to exclude the thermal effect. The other was associated with the mantle structure, as defined by temperature; we used  $\alpha$  with the non-zero value. Table 1 lists the remaining thermal properties considered in our model.

The bottom boundary and most of the side walls have free-slip boundary conditions. The temperature was fixed at initially inverted values at the bottom, and the zero heat flux conditions were assumed on the closed sides.

Compressional boundary tractions were applied to the lithospheric portion of the domain's western side wall while the rest of the boundary was open (Fig. 4b). To construct this boundary condition, the compressional boundary tractions were the sum of the uniform compressional traction and normal tractions extracted from the western wall of case x-1. This boundary condition was introduced because the KP is characterized by mostly east–west compression, at least at crustal depths, based on previous studies (Jin *et al.* 2006; Rhee & Kim 2011; Soh *et al.* 2018), including the World Stress Map (Heidbach *et al.* 2018). The east–west compression of the region is attributed to the India–Asia collision and the subduction of the Pacific and Philippine Sea plates (Jolivet *et al.*

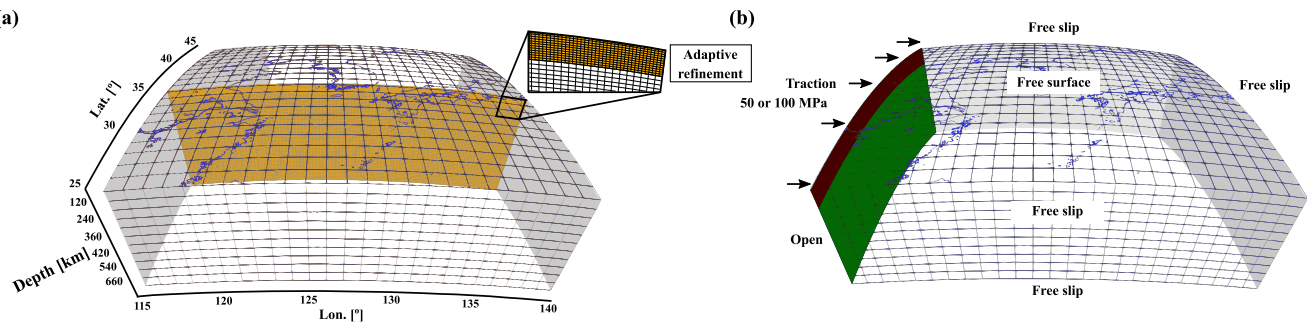


**Figure 4.** (a) Model domain with dimensions. The actual computational mesh is shown on a vertical section along 35°N. Coastlines of the region are drawn on the top of the model domain. (b) Boundary conditions annotated on the model domain. Black arrows next to the west boundary represent the direction of traction for east–west compression. Traction were applied only on the dark red area of the west boundary while the green area is an open boundary.

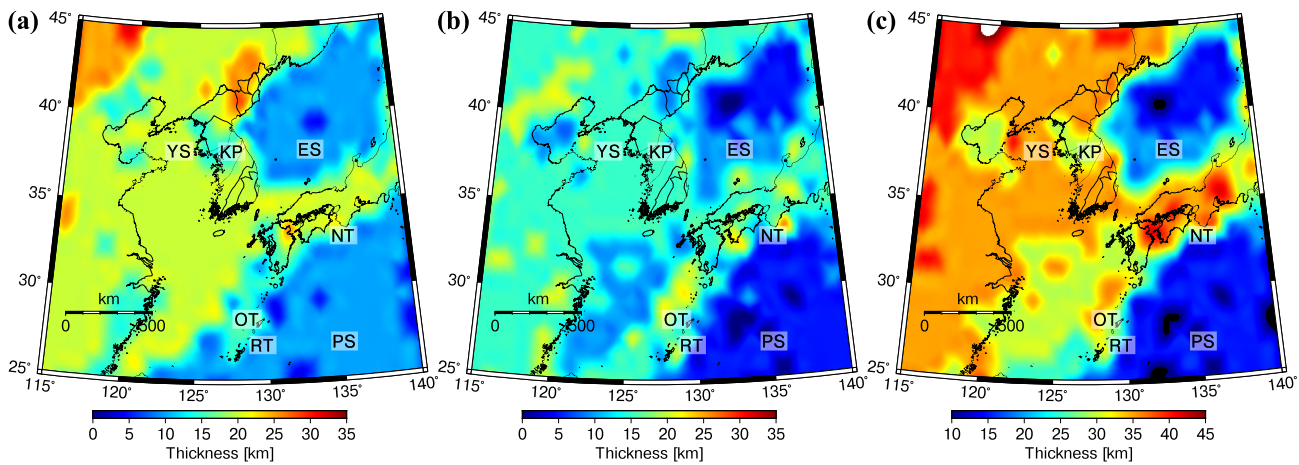


**Figure 5.** Thickness of the (a) upper crust, (b) lower crust and (c) total crust from CRUST1.0 (Laske *et al.* 2013). Refer to Fig. 1(a) for abbreviation definitions.

**Table 1.** Material properties of the crustal layers and upper mantle.

Property	Symbol	Upper crust <sup>a</sup>	Lower crust <sup>b</sup>	Mantle <sup>c</sup>
Density [kg m <sup>-3</sup> ]	P	2608	2915	3300
Specific heat [J kg <sup>-1</sup> K <sup>-1</sup> ]	C <sub>p</sub>	800	800	1250
Thermal expansion coefficient [1 K <sup>-1</sup> ]	$\alpha$	0	0	$3.0 \times 10^{-5}$
Thermal conductivity [W m <sup>-1</sup> K <sup>-1</sup> ]	k	2.5	2.5	3.3
Rheological parameters for diffusion creep				
Grain size [m]	M	$1.0 \times 10^{-3}$	$1.0 \times 10^{-3}$	$1.0 \times 10^{-3}$
Pre-exponential factor [Pa <sup>-n</sup> m <sup>mdiff</sup> s <sup>-1</sup> ]	A	$5.00 \times 10^{-51}$	$5.00 \times 10^{-51}$	$2.37 \times 10^{-15}$
Grain size exponent	m <sup>diff</sup>	3.0	3.0	3.0
Activation energy [J mol <sup>-1</sup> ]	E	0	0	$375 \times 10^3$
Activation volume [m <sup>3</sup> mol <sup>-1</sup> ]	V	0	0	$10.0 \times 10^{-6}$
Rheological parameters for dislocation creep				
Pre-exponential factor [Pa <sup>-n</sup> s <sup>-1</sup> ]	A	$8.57 \times 10^{-28}$	$7.13 \times 10^{-28}$	$6.52 \times 10^{-16}$
Stress exponent	n	4.0	3.0	3.5
Activation energy [J mol <sup>-1</sup> ]	E	$223 \times 10^3$	$345 \times 10^3$	$530 \times 10^3$
Activation volume [m <sup>3</sup> mol <sup>-1</sup> ]	V	0	0	$18.0 \times 10^{-6}$
Angle of internal friction	$\phi$	30.0	30.0	30.0
Cohesion [MPa]	c	20.0	20.0	20.0

Values taken from a: Rutter & Brodie (2004), b: Rybacki & Dresen (2000) and c: Hirth & Kohlstedt (2003).

2018). The applied tractions have magnitudes of 50 and 100 MPa. These values correspond to deviatoric stress magnitudes for strain rates of  $2.5 \times 10^{-17}$  and  $5 \times 10^{-17}$  ( $1\text{ s}^{-1}$ ), respectively and a lithospheric viscosity of  $10^{24}$  Pa·s. The assumed strain rate magnitudes were derived from the changes in the east–west velocity of 1.09 and  $2.18\text{ mm yr}^{-1}$  over an angular distance of  $25^\circ$ , which is approximately 2775 km. These velocities are on the same order of magnitude as the relative plate velocities estimated at 0.27 to  $2.78\text{ mm yr}^{-1}$  around the KP (Jin *et al.* 2006). The thickness of the lithosphere was set to 120 km based on the high viscosity ( $\geq 10^{23}$  Pa·s) mantle (Fig. S2) under the averaged reference geotherm (Fig. S1). The zero-heat flux condition was assumed on the western sidewall.

The top boundary was treated as a free surface because this is more realistic than applying the free-slip condition (Rose *et al.* 2017; Heister *et al.* 2020). In practice, several numerical time steps can be used until an initially flat top surface reaches a quasi-isostatic state as the top surface deforms in response to vertical tractions in ASPECT's Arbitrary Lagrangian-Eulerian framework (Rose *et al.* 2017). Surface topography arrives at a near-isostatic equilibrium within 200 kyr in our models (Fig. S3). However, this forward time-stepping must not be mistaken as a process of predicting the state of the region after 200 kyr from the present. In addition, topography on a deforming free surface should be distinguished from dynamic topography (i.e.  $\frac{-\sigma_{zz}}{\rho g}$ ) conventionally used in a geodynamic model with a free-slip top boundary (e.g. Saxena *et al.* 2021). The temperature was fixed at 273 K on this boundary.

Six models were constructed (Table 2) to systematically explore the effects of heterogeneities in the crust and upper mantle, as well as far-field tectonic stresses. The models were labelled as case  $x-y$  ( $x = 1$  or 2 and  $y = 1, 2$  or 3). Case 1- $y$  had variations in its crustal thickness and mantle temperature field following the averaged reference geotherm, instead of a tomography-based non-uniform temperature field. Case 2- $y$  differed from case 1- $y$  in that it had an inverted heterogeneous temperature field in the upper mantle. The second index in the model label indicates one of three kinematic boundary conditions. In case  $x-1$ , all of the sidewalls and bottom surface had free-slip boundary conditions while the top boundary was a free surface. Cases  $x-2$  and  $x-3$  differed from case  $x-1$  in that they had the compressional traction boundary condition on the western sidewall. The magnitude of the traction was 50 MPa for case  $x-2$  and 100 MPa for case  $x-3$ . The Supporting Information (Text S1) provide more details on our numerical models. Table 2 lists all of the models presented in this study with their defining characteristics. The model input files are made available through a data repository for the reproducibility of our work (Lee 2021).

### 2.3. Quantification of spatial correlation for modelled results with seismicity

As the square root of the second invariant of the deviatoric stress ( $\sqrt{\sigma_{II}}$ , ‘second invariant of stress’ hereafter) represents the ‘mantle flow stress’ (Becker *et al.* 2015), we analysed this quantity using our numerical models to investigate its spatial correlation with the upper crustal seismicity of the KP. We took the average of  $\sqrt{\sigma_{II}}$  over a depth range of 0–20 km to represent the crustal seismicity.

To quantify the spatial correlations between the modelled quantities and seismicity of the KP, Molchan curves (Molchan & Kagan 1992) and their skills (Becker *et al.* 2015; Saxena *et al.* 2021) were used. A model-derived quantity (e.g.  $\sqrt{\sigma_{II}}$ ) was normalized via min-max normalization and expressed as a fraction of ‘occupied’ space. The fraction of earthquakes ( $M_L \geq 3$ ) that occurred outside

the space occupied by a predictor of less than a certain value was computed and referred to as the fraction of missed earthquakes. A Molchan curve is a plot of the fractions of missed earthquakes as a function of the fractions of occupied space. The skill ( $S$ ) of a Molchan curve is defined as 0.5 subtracted from the area under a Molchan curve (Becker *et al.* 2015; Saxena *et al.* 2021). The minimum of a predictor has a zero fraction of occupied space. As the minimum will ‘miss’ all of the earthquakes, the corresponding fraction of missed earthquakes must be 1. The occupied space fraction of the predictor’s maximum is 1. As the occupied space will include all earthquakes, the fraction of missed earthquakes must be 0. For this reason, a Molchan curve is bounded by  $[0, 1] \times [0, 1]$ . For a Molchan curve with a spatially uniform distribution of earthquakes,  $S$  will be equal to zero. The theoretical maximum and minimum of  $S$  are 0.5 and  $-0.5$ . Generally, a greater magnitude for  $S$  represents a better spatial correlation between a predictor and a given earthquake distribution.

## 3. RESULTS

### 3.1. Velocity, temperature and viscosity fields

The surface velocity field of case 1-1 reflects the variations in the crustal thickness (Fig. 5), converging in the relatively thin-crust area, such as the ES (Fig. 6a), and showing small ( $< 1\text{ mm yr}^{-1}$ ) magnitudes in thick-crust areas, such as the KP and YS. In cases 1-2 and 1-3, the eastwards component of velocity was stronger at the top surface than in case 1-1 due to traction on the western sidewall (Figs 6b and c). Moreover, the north–south variations in the flow along the western sidewall were driven by the gradually decreasing gravitational potential energy (GPE) along the latitude at the sidewall because the crust continues to thicken (Figs 6a–c).

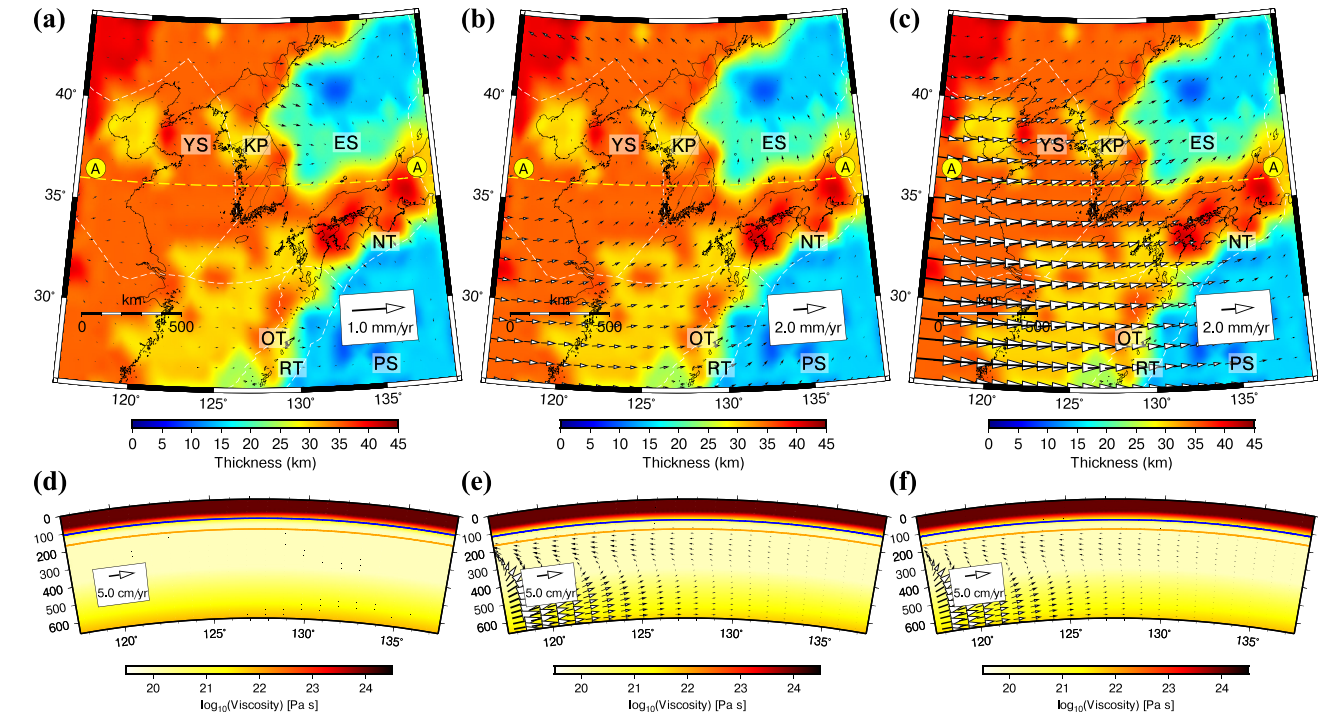
A  $36^\circ\text{N}$  transection of the viscosity field of case 1-1 (Fig. 6d) showed that the lithosphere has a viscosity ranging from  $10^{23}$  to  $10^{24}$  Pa·s from the top surface to 120 km, where temperatures are  $< 1300\text{ K}$ , whereas the asthenosphere ranged from  $10^{20}$  to  $10^{21}$  Pa·s at depths from 120 to 400 km. Below 400 km to the bottom boundary, the viscosity increased to approximately  $10^{22}$  Pa·s. Velocity magnitudes were  $< 0.5\text{ mm yr}^{-1}$  (Fig. 6d). The traction-supported open western boundary in cases 1-2 and 1-3 allowed for vigorous inwards flows on the lower part of the western side due to volume conservation and heterogeneous variations in the GPE driven by variations in the crustal thickness (Figs 5 and 6e and f). Westwards and eastwards components were dominant in the modelled asthenosphere (i.e. 120–270 km) and beneath the asthenosphere, respectively (Figs 6e and f).

Convergent flows in the Okinawa Trough dominated at the surface of case 2-1, with heterogeneities in the upper mantle (Fig. 7a). At a depth of 100 km, lateral flows were strong in the northeastern part of the domain; these flows were associated with the positive buoyancy and relatively hot bodies present in the upper mantle (Figs 3a and 7b). Furthermore, we observed a correlation among the upper mantle low-velocity anomalies, high-temperature anomalies, relatively low density, and areas characterized by Cenozoic volcanism (Figs 2a, 3a and 7b). In contrast, lateral flows were significantly weaker in the negative buoyancy and relatively cold lithosphere to the west of the KP at the same depth (Figs 3a and 7b).

High-viscosity features in the vertical transections of case 2-1 (Figs 7c–f) corresponded to variable thicknesses in the lithosphere, subducting slabs, gaps in the subducting slabs and stagnant slabs at the 660-km discontinuity. Latitudinal transections AA and BB

**Table 2.** Case descriptions for numerical simulations.

Model	Crust thickness	Temperature	B.C.	Chemical composition of mantle
Case 1–1	CRUST1.0	Laterally uniform	Free kinematic	-
Case 1–2	CRUST1.0	Laterally uniform	50 MPa traction	-
Case 1–3	CRUST1.0	Laterally uniform	100 MPa traction	-
Case 2–1	CRUST1.0	Inverted from Tao <i>et al.</i> (2018)	Free kinematic	Average
Case 2–2	CRUST1.0	Inverted from Tao <i>et al.</i> (2018)	50 MPa traction	Average
Case 2–3	CRUST1.0	Inverted from Tao <i>et al.</i> (2018)	100 MPa traction	Average

**Figure 6.** Spatial distribution of the velocity and crustal thickness for (a–c) case 1–y ( $y = 1, 2$  and 3) at the surface, viscosity in (d–f) for case 1–y ( $y = 1, 2$  and 3) for transects (c) along  $36^\circ\text{N}$ . Plate boundaries are shown with white dashed lines (Bird 2003). Blue and orange contours represent temperatures of 1300 and 1600 K, respectively.

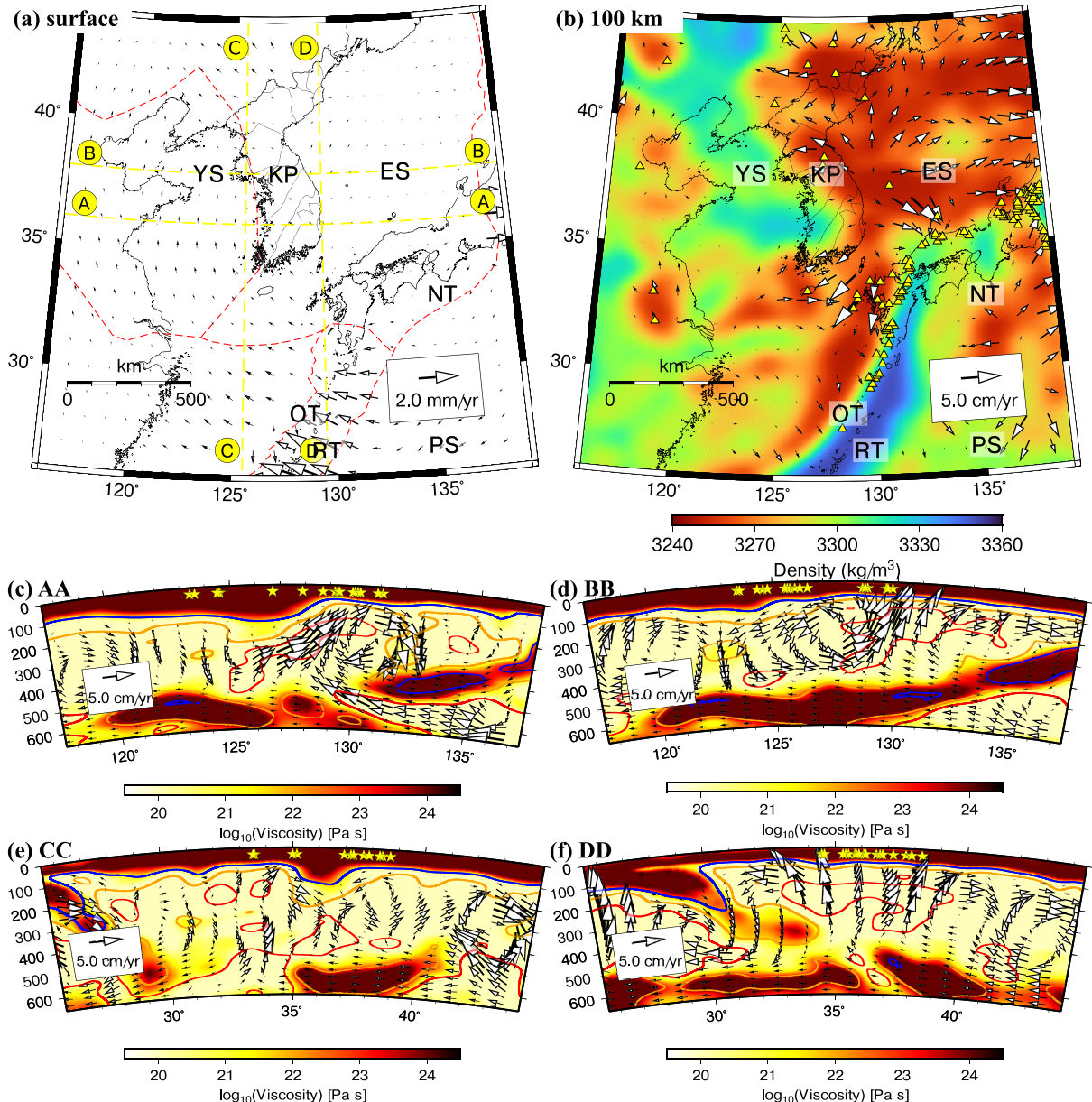
showed multiple convection cells. A particularly strong convection cell existed at a depth of 200–300 km and at approximately  $130^\circ\text{E}$ , which is associated with a high-temperature body present beneath the eastern KP (indicated by the red contours in Figs 7c–d). In longitudinal transection CC (Fig. 7e), mantle flows were mostly associated with slabs, hot anomalies, and lithosphere thickness. Vigorous upwelling in the eastern KP, as observed in transections AA and BB, was also present in longitudinal transection DD (Fig. 7f). These upwellings, as shown in several transections, are also associated with areas characterized by Cenozoic volcanism (Figs 7b–f). This finding is consistent with previous results; a steep gradient in the lithospheric thickness can induce and maintain localized mantle upwelling and decompressional melting along the margins of the relatively thick lithosphere (King & Anderson 1998; Song *et al.* 2020).

Fig. 8 shows the velocity, temperature, and viscosity fields in case 2–2. At the surface, the velocity fields in case 2–2 showed flows parallel to the plate boundary in the western KP and the

northeastwards and eastwards flows in the eastern KP (Fig. 8a), whereas the velocity fields were similar to those in case 2–1 at a depth of 100 km (Figs 7b and 8b). The viscosity structures in case 2–2 were almost identical to those in case 2–1 (Figs 7c–f and 8c–f). Transections AA to DD showed velocity fields that were similar to those in case 2–1 because flows driven by applied tractions were not higher than those driven by buoyancy force in the entire depth range (Figs 8c–f). The temperature and viscosity fields in case 2–3 resembled those in case 2–2, but the velocity fields showed overall eastwards flow components because the magnitude of the compressional traction was 100 MPa, which was two-fold higher than 50 MPa in case 2–2 (Fig. S4).

### 3.2. Surface topography

The surface topographies of case 1s exhibited a correlation with the crustal thickness (Fig. 5c) through isostasy based on Airy's assumption (Figs 9a–c). The eastern margin of the KP and ES,



**Figure 7.** Spatial distribution of the velocity, density, and viscosity in case 2–1 at (a) the surface; (b) a depth of 100 km and on transects (c) AA along 36°N, (d) BB along 38°N, (e) CC along 125.5°N and (f) DD along 129.5°N. Plate boundaries are shown with red dashed lines (Bird 2003). Yellow triangles in (b) indicate Cenozoic volcanism (Global Volcanism Program 2013). Blue, orange, and red contours represent temperatures of 1300, 1600 and 1900 K, respectively. Yellow stars indicate epicentres, which are  $\pm 1^\circ$  adjacent to the transects and  $\geq M_L 4.0$ . Note that the depth of the earthquakes was fixed at 20 km for visualization, and the velocity fields were resampled by taking the average velocity in  $1^\circ \times 1^\circ$  bins in map view and  $1^\circ \times 30$  km for vertical transects. Refer to Fig. 1(a) for abbreviation definitions.

which have a thin crust, is below sea level while the broad region to the west of the KP has a thicker crust and is higher than the eastern region. The root mean square errors (RMSEs) between the observation and modelled topography of cases 1–1 to 1–3 were 1015, 416 and 425 m, respectively.

The surface topography of case 2s had smaller differences in the observed topography (Fig. 1a) than that of case 1s. The RMSEs between the observation and modelled topographies were 352 and 360 m in cases 2–2 and 2–3, respectively, which were 416 and 425 m in cases 1–2 and 1–3, respectively. The traction-free models, that is cases 1–1 and 2–1, had overall greater RMSEs, at 1015 and 694 m, respectively, than those with traction, but the

surface topography of case 2–1 was more similar to the observed topography.

The mean elevation was 750 m higher in the models without the traction boundary conditions, that is cases 1–1 and 2–1 (Fig. 9a and d), than in those with them (Figs 9b, c, e and f). When all sides were closed to outwards flows in cases 1–1 and 2–1, the surface topography received greater dynamic support.

### 3.3. Second invariant of the deviatoric stress

The spatial distributions of  $\sqrt{\sigma_{II}}$  in case 1s did not correlate well with the seismicity (Figs 10a–c). Specifically, the three models showed

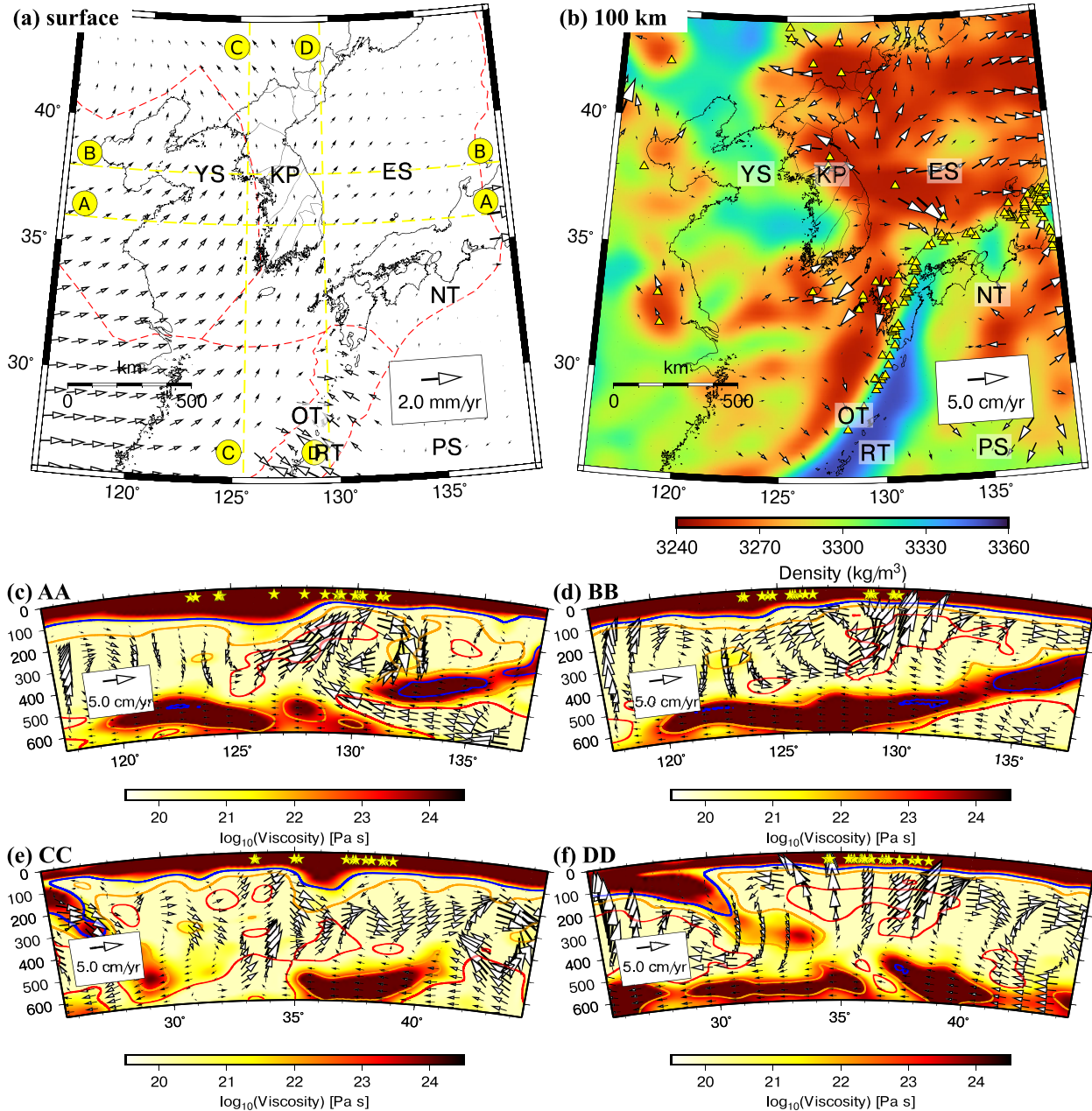


**Figure 8.** Spatial distribution of the velocity, density, and viscosity in case 2–2 at (a) the surface; (b) a depth of 100 km; and on transects (c) AA along 36°N, (d) BB along 38°N, (e) CC along 125.5°N and (f) DD along 129.5°N. Plate boundaries are shown with red dashed lines (Bird 2003). Yellow triangles in (b) indicate Cenozoic volcanism (Global Volcanism Program 2013). Blue, orange, and red contours represent temperatures of 1300, 1600 and 1900 K, respectively. Yellow stars indicate epicentres, which are  $\pm 1^\circ$  adjacent to the transects and  $\geq M_L 4.0$ . Note that the depth of the earthquakes was fixed at 20 km for visualization, and the velocity fields were resampled by taking the average velocity in  $1^\circ \times 1^\circ$  bins in map view and  $1^\circ \times 30$  km for vertical transects. Refer to Fig. 1(a) for abbreviation definitions.

100–120 MPa for  $\sqrt{\sigma_{II}}$  in the ES and around Ulleung volcanic Island (UI), but the seismicity was relatively low in these areas (Figs 10a–c). Additionally, the magnitudes were consistently low or moderate inside the KP (Figs 10a–c).

The  $\sqrt{\sigma_{II}}$  for case 2–1 showed western and eastern highs of 140–160 MPa and a central low of 40 MPa throughout the geologic provinces of Pyeongnam Basin (PB) and Gyeonggi Massif (GM, Fig. 10d). The distribution yielded 100 MPa for  $\sqrt{\sigma_{II}}$  on Jeju volcanic Island (JI, Fig. 10d).

The boundary tractions applied in cases 2–2 and 2–3 increased  $\sqrt{\sigma_{II}}$  in the western KP and YS while  $\sqrt{\sigma_{II}}$  decreased in the eastern KP and ES (Figs 10e and f). Particularly, case 1s showed low (10–70 MPa) stress in the YS, whereas case 2s showed relatively high stress (90–240 MPa) in the YS but low stress in the ES around the UI, where seismic activity is low. Additionally, cases 2–1 and 2–2 showed high stress along the eastern margin of the KP, which also follows the distribution of  $M_L \geq 4$  earthquakes (Figs 10d and e).

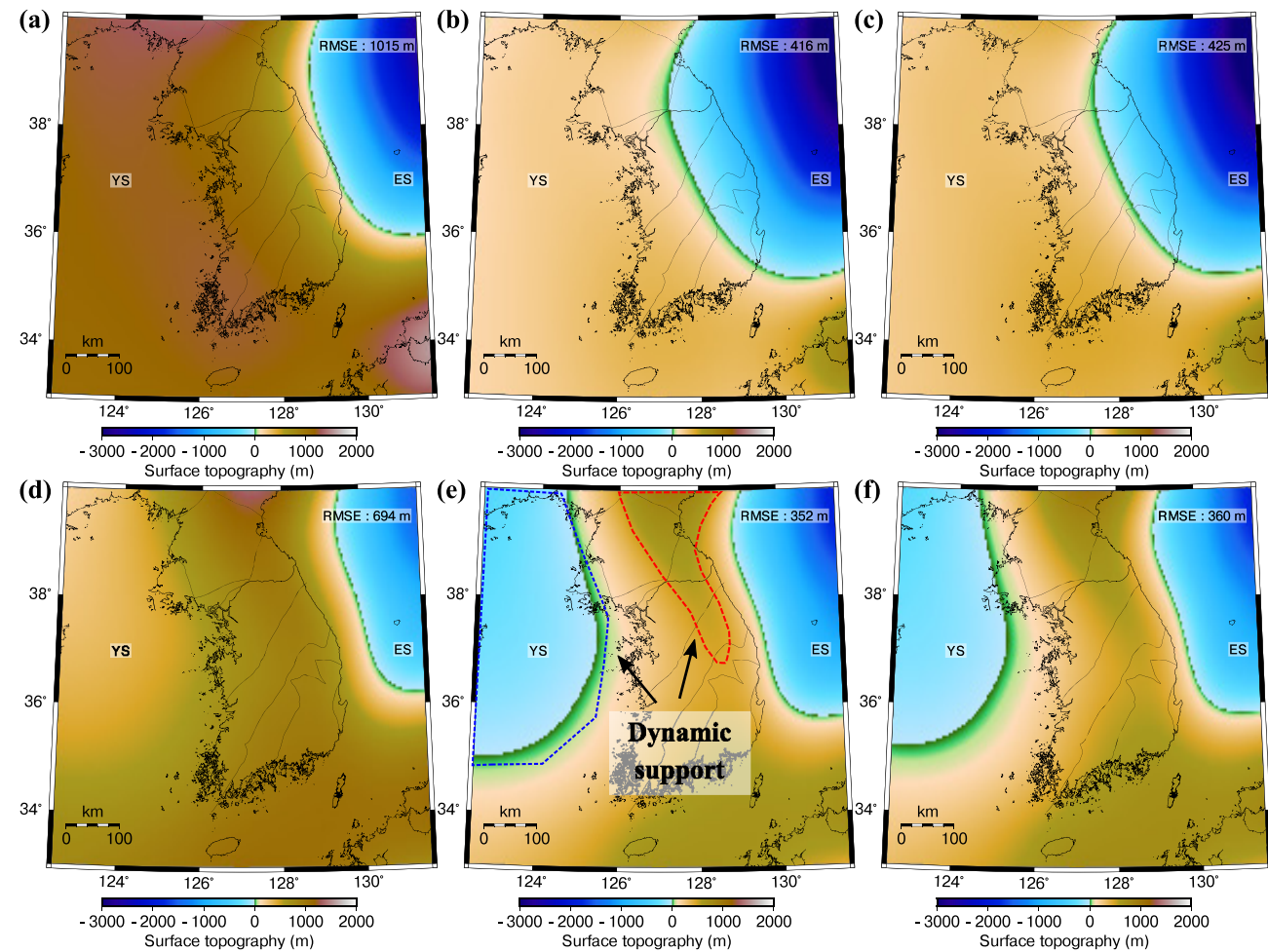


**Figure 9.** Surface topography of (a–c) case 1-y ( $y = 1, 2$  and 3) and (d–f) case 2-y ( $y = 1, 2$  and 3). The root mean square errors (RMSEs) between the observations (Tozer *et al.* 2019) and model predictions are included. Refer to Fig. 1(a) for abbreviation definitions. Dynamic support in (e) means that topography isostatically supported through crustal thickness variations is not included (Steinberger 2016).

The Molchan curves for case 1s had  $S$  values of 0.10, 0.08 and 0.12 (Fig. 11a) while these values for case 2s were 0.21, 0.21 and 0.14 (Fig. 11b).

### 3.4 Orientation of compressive horizontal maximum stress

The orientation of the horizontal maximum compressive stress ( $\varphi_H$ ) in case 1–1 showed that the north–south components are dominant in the KP (Fig. 12a). With the upper-mantle heterogeneities in case 2–1, the east–west components are dominant in the western KP, but the north–south components are dominant in the eastern KP. The models with the 50 MPa traction (cases 1–2 and 2–2) exhibited increased magnitudes in the east–west component in  $\varphi_H$  relative to case x–1s (Figs 12b and e). The degree of east–west alignment was greater in the models with 100 MPa traction (Figs 12c and f).

Case 1–1 yielded a value of  $24.7^\circ$ – $87.1^\circ$  for  $\Delta\varphi$ , which is the absolute deviation in  $\varphi_H$  from those inverted from earthquake focal mechanisms by Soh *et al.* (2018) ( $\varphi_{\text{inv}}$ ). The  $\Delta\varphi$  values of case 2–1 were  $6.3^\circ$ – $36.2^\circ$  in the western KP and  $21.2^\circ$ – $83.5^\circ$  in the eastern KP. The mean  $\Delta\varphi$  value of case 2–1 was  $18.9^\circ$  smaller than that of case 1–1.

The applied traction yielded a value for  $\varphi_H$  similar to  $\varphi_{\text{inv}}$ :  $\Delta\varphi$  was  $0.3^\circ$  and  $46.7^\circ$  in case 1–2 and 1–3, respectively, and  $0.9^\circ$  and  $77.4^\circ$

in cases 2–2 and 2–3, respectively. The  $\Delta\varphi$  values were smaller in cases 1–2 and 1–3 than in their counterparts of case 2s because the upper-mantle heterogeneities added non-uniform complexity to the stress fields in the latter cases (Figs 12b, c, e and f).

## 4. DISCUSSION

### 4.1 Analysis of results

A comparison of the surface topographies of cases 1s and 2s confirms the dynamic contributions from the lithospheric and upper-mantle heterogeneities. The YS region, which is below sea level in cases 2–2 and 2–3, but not in cases 1–2 and 1–3 (Figs 9e and f), indicates a mantle origin for the region's relatively low topography. Another indicator of the dynamic contribution to the surface topography in cases 2–2 and 2–3 is a mountain belt along the eastern coastline (Figs 9e and f), which is below sea level in cases 1–2 and 1–3 (Figs 9b and c). If the eastern mountain belt is solely supported by crustal isostasy, as in case 1s, the belt would require a thickness of  $>40$  km. However, the crustal models consistently indicate that the crust thins eastwards from 35 to 25 km (Chang & Baag 2005; Laske *et al.* 2013; Fig. 5c).

The  $\sqrt{\sigma_{II}}$  value in cases 2–1 and 2–2 shows eastern highs that can be attributed to lithospheric and upper-mantle structures, rather

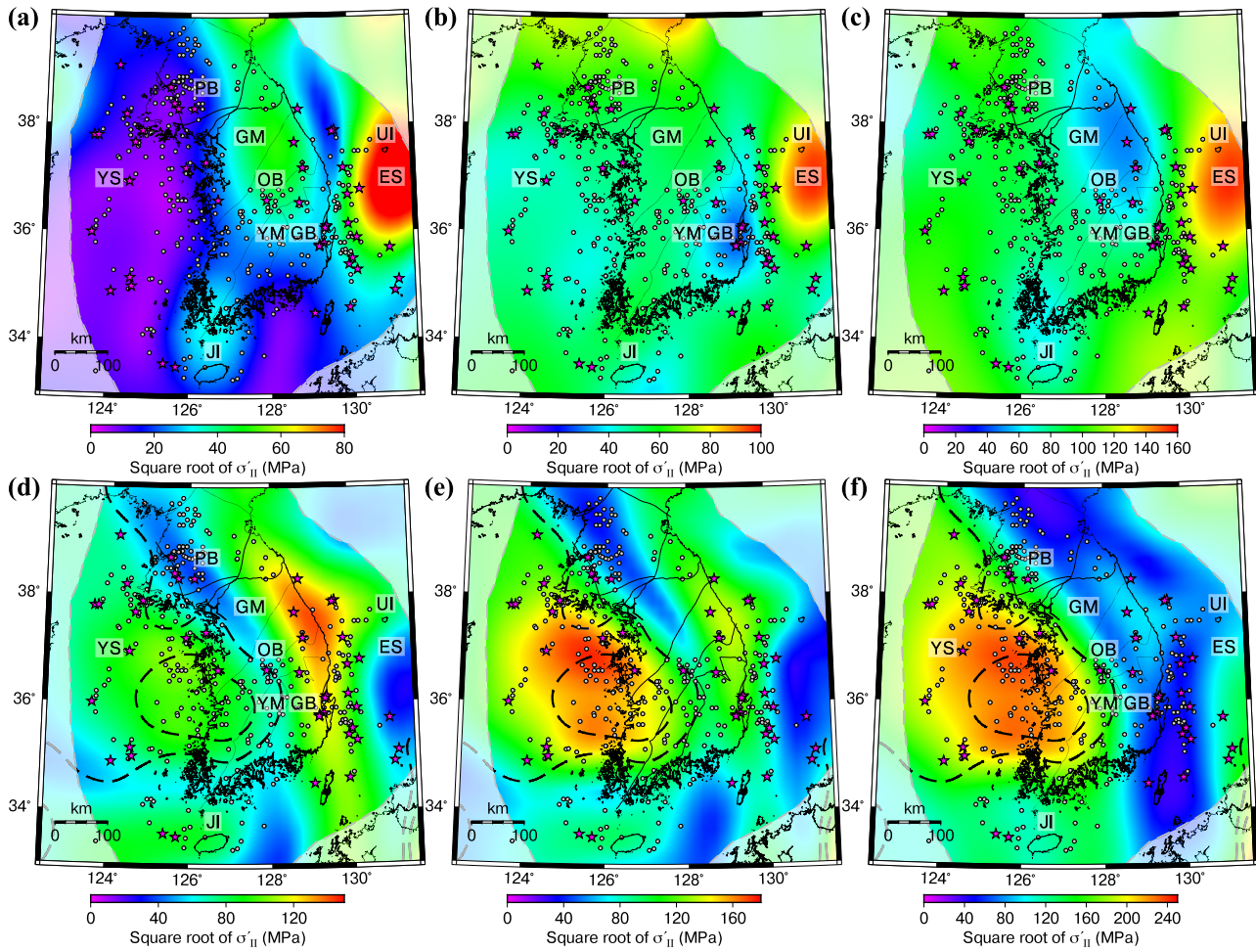


**Figure 10.** Spatial distribution of the vertical averaged (surface to 20 km depth)  $\sqrt{\sigma_{II}'}$  for (a–c) case 1-y ( $y = 1, 2$  and 3) and (d–f) case 2-y ( $y = 1, 2$  and 3), respectively. Events  $\geq M_L$  3.0 and  $M_L$  4.0 are indicated by white dots and magenta stars, respectively. Non-shaded regions show the calculations of the other Molchan curves. The black-dashed lines in panels (d–f) represent inferred lithospheric thickness of 97 and 139 km with the 1300 K isotherm. ES, East Sea (Sea of Japan); GB, Gyeongsang Basin; GM, Gyeonggi Massif; JI, Jeju volcanic Island; OB, Okcheon Belt; PB, Pyeongnam Basin; UI, Ulleung volcanic Island; YM, Yeongnam Massif and YS, Yellow Sea.

than variations in the crustal thickness (Figs 10d and e). The eastern regions, with relatively large magnitudes of  $\sqrt{\sigma_{II}'}$ , are associated with the particularly strong convection cell at depths of 200–300 km and at approximately 130°E in the ES (Figs 7f and 8f). Additionally, the  $M_L \geq 4$  events occurred above that structure (Fig. 8f). Although the eastern highs of  $\sqrt{\sigma_{II}'}$  coincide with the COT within the crust (Fig. 5), which can contribute to crustal seismicity (e.g. Soto-Cordero *et al.* 2018), the influence of the COT on the seismicity of this region appears to be weak because case 1s, with crustal thickness variations, consistently shows smaller  $S$  values for  $\sqrt{\sigma_{II}'}$  than case 2s with respect to the  $M_L \geq 3$  earthquakes (Figs 10 and 11). Becker *et al.* (2015) estimated a quantity self-evidently correlated with an earthquake distribution in the western United States, which yielded an  $S$  value of 0.42 as an upper bound for Molchan analysis. Moreover, they conducted Monte Carlo simulations using spatial fields of random numbers as a lower bound for Molchan analysis. They then estimated  $S$  values of  $>0.13$ , allowing for correlations of the earthquake distributions, and suggested the greatest  $S$  value, which was approximately 0.13 greater than the lower bound, as a superior correlation. In a similar approach, a Molchan analysis of the seismic moment density (Fig. S5), which is a quantity self-evidently

correlated with the earthquake distribution, yielded an  $S$  value of 0.43. Random numbers between zero and one in the KP were generated 1000 times and the maximum  $S$  value was 0.09, which we consider as the lower bound for non-randomness. The  $S$  values for  $\sqrt{\sigma_{II}'}$  in cases 2–1 to 2–3 were 0.21, 0.21 and 0.14, respectively, all of which were  $>0.09$ . The  $S$  values in cases 1–1 to 1–3 were 0.10, 0.08 and 0.12, respectively, which were all similar to 0.09. As a result,  $\sqrt{\sigma_{II}'}$  in cases 2–1 and 2–2 could be a superior predictor according to Becker *et al.* (2015).

We focus on case 2s in the remainder of this section because we find that dynamic contributions are necessary and the statistical scores for case 2s, with a heterogeneous mantle, improved relative to those of case 1s. The  $\Delta\varphi$  in case 2s in the western KP was not variable regardless of the applied tractions in the east–west direction while the  $\Delta\varphi$  in case 2s in the eastern KP was smaller with the applied tractions and  $\varphi$  around the epicentre of the Gyeongju earthquake was consistent with the  $P$ -axis of the Gyeongju earthquake by increasing the applied tractions (Figs 12d–f). Therefore, we divided the KP into the western and eastern branches to investigate the contributions of the heterogeneities to the seismicity of each region.

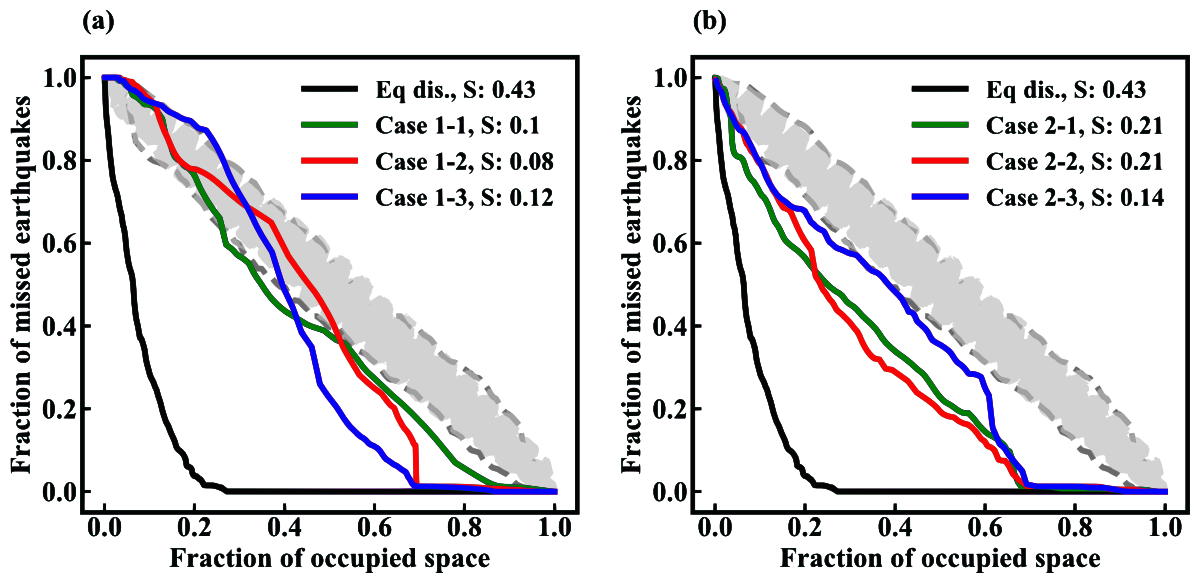


**Figure 11.** Analysis of the  $S$  values for the seismicity of the KP and  $\sqrt{\sigma'_{II}}$  for (a) case 1 and (b) case 2 using Molchan curves, where the diagonal grey area indicates a random prediction for the low bound and the black line represents the earthquake distributions for the upper bound. Green, red and blue lines represent  $\sqrt{\sigma'_{II}}$  for submodels of cases 1s and 2s with the  $S$  value.

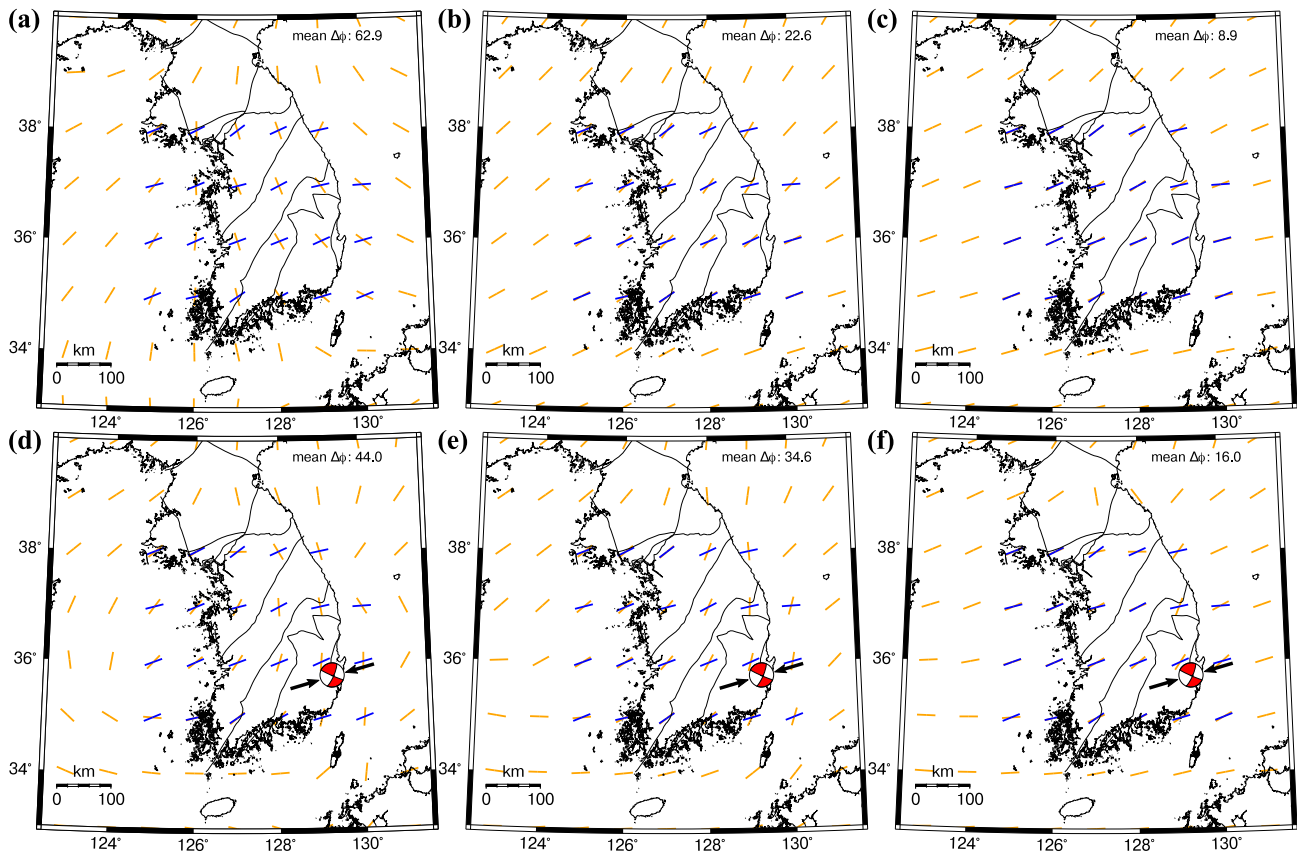


**Figure 12.** Orientation of the maximum horizontal compression ( $\varphi_H$ , orange bars) of (a–c) case 1–y ( $y = 1, 2$  and 3) and (d–f) case 2–y ( $y = 1, 2$  and 3), respectively, with stress inversions using the instability method (Vavryčuk 2014) from Soh *et al.* (2018) ( $\varphi_{inv}$ , blue bars). The mean deviation of the  $\varphi_H$  from  $\varphi_{inv}$  is given in the legend,  $\Delta\varphi$ . Note that the orientation of the maximum horizontal stresses of cases 1s to 2s was resampled by taking the average of the orientations in  $1^\circ \times 1^\circ$  bins in map view from the surface to a depth of 20 km, followed by vertically taking the average of the orientations for  $\varphi_H$  in the upper crust. The focal mechanism for the  $M_L 5.8$  Gyeongju earthquake (Kim *et al.* 2016) is plotted along the  $P$ -axis in panels (d–f).

## 4.2 Seismicity in the western KP and YS

All three quantities that were compared with the observations suggest the need for mantle heterogeneities in the western KP and YS. The dynamic contribution to the surface topography is required for the YS as a subaerial area (Figs 9d–f). The heterogeneities in the mantle in this region significantly increase the stress in the upper crust; this stress coincides with the observed seismicity (Figs 10d–f). The  $\varphi_H$  value, due to these heterogeneities, agreed with  $\varphi_{\text{inv}}$  value (Figs 12d–f). Additionally, the regional compressive stress reduces the RMSEs of the surface topography and  $\Delta\varphi$ , but also accumulates stress (Figs 9d–f, 10d–f and 12d–f). Therefore, mantle heterogeneities with regional stress contribute to the upper crustal seismicity in the western KP and YS, where cold, dense, and thick lithosphere exists.

An investigation of the viscosity structures in case 2s revealed that many  $M_L \geq 4$  earthquakes (i.e. moderate-sized or greater intraplate earthquakes) do not occur in the thickest part of the lithosphere, but rather in the regions surrounding it (Figs 7c and e, 8c and e and S5c and e).

To clarify the spatial correlation, we inferred that the lithospheric thickness of the KP ranges from 50 to 175 km using the inverted temperature used in case 2s when the 1300 K isotherm was considered as the lithosphere–asthenosphere boundary. We used an average thickness of 88 km as a conceptual boundary between the thick and thin lithosphere (Fig. S6). According to this division, the thick lithosphere has an average thickness of  $118 \pm 21$  km. Assuming a thickness ranging from 97 to 139 km as the edge of the thick lithospheric core, we found that most of the  $M_L \geq 4$  events in the western KP were located within this part of the lithosphere (Figs 10 and S6) and not in the thickest part. Such a close correspondence between the crustal seismicity and lithospheric thickness distribution is indeed expected because the strength of the seismogenic upper crust, capped by the brittle strength (i.e. Byerlee's law), is insignificant relative to the overall strength of lithosphere.

Also, this relationship between moderate-sized seismicity and the lithospheric thickness has been observed previously by several authors in other stable continental regions (SCRs), such as eastern North America, the Siberian shield, the Brazilian shield and the Congo craton (e.g. Craig *et al.* 2011; Mazzotti 2007; Sloan *et al.* 2011; Mooney *et al.* 2012). Additionally, by quantifying the lithospheric strength based on seismic tomography models in North America, Tesauro *et al.* (2015) found that intraplate seismicity does not show a clear association with high-strength craton cores, but rather with their edges. The intraplate seismicity in eastern North America shows that few events have occurred along known geological lineaments (Mazzotti 2007). So, Mooney *et al.* (2012) assumed that the difference in the strength of the lithosphere produced the earthquake cluster around the edge of the craton.

These findings could have led to the realization that lateral variations in the lithospheric thickness and the difference in the strength of the lithosphere are more important than inherited weaknesses in a region with a relatively thick lithosphere. Additionally, previous geodynamic simulations predicted the greatest stresses or tractions within high-viscosity bodies such as cratonic cores and shields (e.g. Ghosh *et al.* 2013; Ghosh *et al.* 2019; Paul *et al.* 2019), as  $\sqrt{\sigma_{\text{II}}}$  in case 2s in the western KP increased and accumulated in the thick lithosphere with traction even at a low strain rate because stress was the product of viscosity and strain rate in this study (Figs 10d–f and S6). Thus, we may suggest that earthquakes in the western KP can be attributed to tectonic stresses concentrated along the edges of

relatively strong and thick structures, which are the boundaries of the lithospheric strength.

## 4.3 Seismicity in eastern KP and ES

A trade-off, which can decide whether the mantle heterogeneities contribute to the crustal seismicity, occurred in case 2s. A dynamic contribution to the surface topography was necessary to build the eastern mountain belt and reduce the RMSEs of the surface topography compared with the counterparts of case 1s (Fig. 9). The stresses in the upper crust in cases 2–1 and 2–2 coincide with the observed seismicity. Also, cases 2–1 and 2–2 had the highest  $S$  value (Figs 10d and e and 11b), but the  $\varphi_H$  values of cases 2–1 and 2–2 were highly deviated with the  $\varphi_{\text{inv}}$  values (Figs 12d and e). In contrast, the stress in the upper crust in case 2–3 does not coincide with the observed seismicity; case 2–3 also had the lowest  $S$  value among the different cases in 2s (Figs 10f and 11b), but was consistent with the  $\varphi_{\text{inv}}$  value and the  $P$ -axis of the Gyeongju earthquake (Fig. 12f). Then, case 2–2 or 2–3 can be a candidate for the best-fitting model depending on which quantities are considered to be more weighted. Therefore, it is unclear whether the stress driven by these heterogeneities directly affects the upper crustal seismicity due to the trade-off, despite a clear correlation between the relatively thin lithosphere and strong upper-mantle upwelling with the observed seismicity (Figs 7f, 8f and S5f).

The stress regime of the eastern KP switched from extension to compression in the middle Miocene (Jolivet *et al.* 1994). Studies on seismic sources have also revealed the prevalence of strike-slip and reverse faulting events rather than normal faulting events in the area along the eastern margin (Rhee & Kim 2011; Choi *et al.* 2012). Kim *et al.* (2018) suggested that backarc rifting and breakup generated the structural lineation with a high-angle dip at the margin while the weakness may have been reactivated by the present stress fields, that is east–west compression (Heidbach *et al.* 2018; Soh *et al.* 2018).

However, reactivations during high-angle reverse faulting events are unfavourably orientated with respect to Anderson's theory (Anderson 1951). Moreover, Sibson (1990) suggested that steep reverse faults require supra-lithostatic fluid pressures for reactivation. An ambient seismic noise tomography of the region, resolved by Lee *et al.* (2015), shows low-velocity anomalies from the continental crust to the uppermost mantle. They interpreted the low-velocity anomalies as mature fold and fault systems in the crust and hot bodies in the uppermost mantle, suggesting the presence of hydrothermal activities in the mature fold and fault systems of this region. Lee *et al.* (2019) reported evidence for hydrothermal activity based on geochemical aspects; dissolved gases in groundwater show significant contribution from the mantle to the  $^3\text{He}/^4\text{He}$  ratio and carbon isotope compositions ( $\delta^{13}\text{C}$ ) of  $\text{CO}_2$  in the southeastern part of the KP.

Therefore, we suspect that the seismicity of the eastern KP may not directly respond to stress driven by upwelling but can be attributed to the present stress fields and mantle-derived multiphase fluid flow (i.e. water and gases) along weak zones.

## 4.4 Limitations

The numerical models presented in this study can be improved in future studies. Absolute plate motions could have been imposed on the models, but we did not use them because the displacements measured by GPS and their signal-to-noise ratio are so small in the KP (Jin *et al.* 2006; Kreemer *et al.* 2014) that the available

absolute plate motion models include large uncertainties (Kreemer *et al.* 2014). As temperature inversion is sensitive to the mineral composition and  $Q$  factors of the mantle (Cammarano *et al.* 2003; Steinberger 2016), different mantle compositions and  $Q$  factors that reflect the possibility of partial melting beneath the ES (Ismail-Zadeh *et al.* 2013) require further analysis. The fast direction of the shear-wave splittings could be useful to constrain upper-mantle flow (Jolivet *et al.* 2018), but we did not use it because the available shear-wave splitting data have high uncertainties (see Supporting Information Text S2).

## 5. CONCLUSIONS

In this study, we calculated the stress fields around the KP using 3-D numerical models, including crustal and upper-mantle heterogeneities, as well as traction boundary conditions, to understand their relationship with the seismic activity of the region. To consider the lateral variations in the crust and upper mantle, we adopted the crustal thickness and density from a crustal seismic velocity model and inverted the upper-mantle seismic velocity anomalies from a regional tomography model onto a temperature field, which determined the structures and density. We then performed a series of numerical simulations using a thermomechanical numerical code (ASPECT) to compute stress fields based on the selected contributing factors, such as the heterogeneities and the traction boundary conditions. The major contributions to the seismicity in the KP derive from regional compression in the east–west direction, and the lithospheric and upper-mantle heterogeneities. The modelled surface topography, mantle flow stress and orientation of maximum horizontal stress derived from the variation in the crustal thickness indicate the need to improve these quantities, which can be realized by considering the lithospheric and upper-mantle heterogeneities. Particularly, we analysed the contributions from these heterogeneities by dividing the areas; the western KP and YS, characterized by a cold, dense and thick lithosphere, and the eastern KP and ES, characterized by a hot, light, and thin lithosphere. The mantle heterogeneities with regional stress contribute to the upper crustal seismicity in the western KP and YS; earthquakes in these regions can be attributed to tectonic stresses concentrated along the edges of the relatively strong and thick structures. In contrast, moderate-sized earthquakes along the eastern KP and in the ES show a clear correlation between the relatively thin lithosphere and strong upper-mantle upwelling; however, whether stress driven by these heterogeneities directly affects upper crustal seismicity remains unclear. This study is the first to link lithospheric and upper-mantle heterogeneities with the seismicity of the KP. Our approach and findings can improve our understanding of the seismicity mechanism in regions with low geodetic strain rates and negligible associations with known tectonic fabrics and crustal thickness variations.

## ACKNOWLEDGEMENTS

We thank the editor, anonymous reviewer, and Dr Fenglin Niu for their constructive comments and suggestions that helped improve our manuscript. We also thank CIG (Computational Infrastructure for Geodynamics) for providing the numerical codes for this study (ASPECT and BurnMan). This study was funded by the Korea Meteorological Institute under Grant KMI 2019–00110. The figures in this paper were generated using Generic Mapping Tools ver. 6.0.0 (<https://www.generic-mapping-tools.org/>), Matplotlib ver. 3.3.4 (<https://matplotlib.org/>), Paraview ver. 5.8.1 (<https://www.paraview.org/>)

(rg) and Inkscape ver. 0.92.5 (<https://inkscape.org/>). There are no conflicts of interest to declare.

## DATA AVAILABILITY

Earthquake event data can be acquired from the Korea Meteorological Administration (KMA; <http://necis.kma.go.kr>). The seismic velocity models are available at IRIS from the IRIS Earth Model Collaboration (EMC; <http://ds.iris.edu/ds/products/emc/>). The temperature inversion procedure was implemented in Python and stored as a Jupyter Notebook (available for download at doi.org/10.6084/m9.figshare.12 512 720). The parameter files used in this study are available online (doi.org/10.6084/m9.figshare.14 045 063.v1).

## AUTHOR CONTRIBUTION STATEMENT

The study was conceptualized by Sungho Lee, Arushi Saxena and Eunseo Choi. Methodology was devised by Sungho Lee, Arushi Saxena and Eunseo Choi. Data curation was done by Sungho Lee and Jung-Hun Song. Investigation, visualization, formal analysis and writing the original draft were done by Sungho Lee. Reviewing and writing of the manuscript was carried out by Sungho Lee, Arushi Saxena, Jung-Hun Song, Junkee Rhee and Eunseo Choi. Junkee Rhee supervised the work and Eunseo Choi was in an advisory role. Funding acquisition was managed by Junkee Rhee.

## REFERENCES

- Anderson, E.M., 1951. *The Dynamics of Faulting and Dyke Formation with Application to Britain*, 2nd edn, 206pp., Oliver and Boyd.
- Bangerth, W., Dannberg, J., Gassmöller, R. & Heister, T., 2020. ASPECT v2.2.0. (version v2.2.0).Zenodo. doi.org/10.5281/ZENODO.3924604.
- Becker, T.W., Lowry, A.R., Faccenna, C., Schmandt, B., Borsa, A. & Yu, C., 2015. Western US intermountain seismicity caused by changes in upper mantle flow, *Nature*, **524**(7566), 458–461.
- Birch, F., 1947. Finite elastic strain of cubic crystals, *Phys. Rev.*, **71**(11), 809–824.
- Bird, P., 2003. An updated digital model of plate boundaries, *Geochim. Geophys. Geosyst.*, **4**(3), 1–52.
- Cammarano, F., Goes, S., Vacher, P. & Giardini, D., 2003. Inferring upper-mantle temperatures from seismic velocities, *Phys. Earth planet. Inter.*, **138**(3–4), 197–222.
- Chang, S.-J. & Baag, C.-E., 2005. Crustal structure in Southern Korea from joint analysis of teleseismic receiver functions and surface-wave dispersion, *Bull. seism. Soc. Am.*, **95**(4), 1516–1534.
- Choi, H., Hong, T.-K., He, X. & Baag, C.-E., 2012. Seismic evidence for reverse activation of a paleo-rifting system in the East Sea (Sea of Japan), *Tectonophysics*, **572–573**, 123–133.
- Choi, S.-H., 2012. Lithospheric mantle beneath the Korean Peninsula: implications from peridotite xenoliths in alkali basalts, *J. Petrol. Soc. Korea*, **21**(2), 235–247 (in Korean with English abstract).
- Cottaar, S., Heister, T., Rose, I. & Unterborn, C., 2014. Burnman: a lower mantle mineral physics toolkit, *Geochim. Geophys. Geosyst.*, **15**(4), 1164–1179.
- Craig, T.J., Jackson, J.A., Priestly, K. & McKenzie, D., 2011. Earthquake distribution patterns in Africa: their relationship to variations in lithospheric and geologic structure, and their rheological implications, *Geophys. J. Int.*, **185**, 403–434.
- Duffy, T.S. & Anderson, D.L., 1989. Seismic velocities in mantle minerals and the mineralogy of the upper mantle, *J. geophys. Res.*, **94**(B2), 1895–1912.
- Fraters, M., Bangerth, W., Thieulot, C., Glerum, A. & Spakman, W., 2019. Efficient and practical Newton solvers for non-linear Stokes systems in geodynamic problems, *Geophys. J. Int.*, **218**(2), 873–894.

- Ghosh, A., Holt, W.E. & Bahadori, A., 2019. Role of large-scale tectonic forces in intraplate earthquakes of central and eastern North America, *Geochem. Geophys. Geosyst.*, **20**(4), 2134–2156.
- Ghosh, A., Holt, W.E. & Wen, L., 2013. Predicting the lithospheric stress field and plate motions by joint modeling of lithosphere and mantle dynamics, *J. geophys. Res.*, **118**, 346–368.
- Glerum, A., Thieulot, C., Fraters, M., Blom, C. & Spakman, W., 2017. Nonlinear viscoplasticity in ASPECT: benchmarking and applications to subduction, *Solid Earth*, **9**(2), 267–294.
- Global Volcanism Program, 2013. Volcanoes of the World, v. 4.10.2 (24 Aug 2021), ed. Venzke, E., Smithsonian Institution. Downloaded on 06 Oct 2021. doi.org/10.5479/si.GVP.VOTW4-2013.
- Goes, S., Govers, R. & Vacher, P., 2000. Shallow mantle temperatures under Europe from P and S wave tomography, *J. geophys. Res.*, **105**(B5), 11 153–11 169.
- Hayes, G.P., Moore, G.L., Portner, D.E., Hearne, M., Flamme, H., Furtney, M. & Smoczyk, G.M., 2018. Slab2, a comprehensive subduction zone geometry model, *Science*, **362**(6410), 58–61.
- Heidbach, O. et al., 2018. The World Stress Map database release 2016: crustal stress pattern across scales, *Tectonophysics*, **744**, 484–498.
- Heister, T., Dannberg, J., Gassmöller, R. & Bangerth, W., 2017. High accuracy mantle convection simulation through modern numerical methods-II: realistic models and problems, *Geophys. J. Int.*, **210**(2), 833–851.
- Heister, T., others. 2020. ASPECT: advanced Solver for Problems in Earth's ConvecTion, User Manual, https://doi.org/10.6084/m9.figshare.4865333.
- Hirth, G. & Kohlstedt, D., 2003. Rheology of the upper mantle and the mantle wedge: a view from the experimentalists, *Geophys. Monogr. Am. Geophys. Un.*, **138**, 83–106.
- Houng, S.E. & Hong, T.K., 2013. Probabilistic analysis of the Korean historical earthquake records, *Bull. seism. Soc. Am.*, **103**(5), 2782–2796.
- Ismail-Zadeh, A., Honda, S. & Tsepelev, I., 2013. Linking mantle upwelling with the lithosphere descent and the Japan Sea evolution: a hypothesis, *Sci. Rep.*, **3**, 1137.
- Jin, S., Li, Z.C. & Park, P.-H., 2006. Seismicity and GPS constraints on crustal deformation in the southern part of the Korean Peninsula, *Geosci. J.*, **10**(4), 491–497.
- Jolivet, L., Faccenna, C., Becker, T., Tesauro, M., Sternai, P. & Bouilhol, P., 2018. Mantle flow and deforming continents: from India-Asia convergence to Pacific subduction, *Tectonics*, **37**, 2887–2914.
- Jolivet, L., Tamaki, K. & Fournier, M., 1994. Japan Sea, opening history and mechanism: a synthesis, *J. geophys. Res.*, **99**(B11), 22237–22259.
- Kang, T.S. & Shin, J., 2009. Shear-wave splitting beneath southern Korea and its tectonic implication, *Tectonophysics*, **471**(3–4), 232–239.
- Kim, H.-J., Jou, H.-T. & Lee, G.H., 2018. Neotectonics of the Eastern Korean Margin inferred from back-arc rifting structure, *Ocean Sci. J.*, **53**, 601–609.
- Kim, Y., Rhie, J., Kang, T.-S., Kim, K.-H., Kim, M. & Lee, S.-J., 2016. The 12 September 2016 Gyeongju earthquakes: 1. Observation and remaining questions, *Geosci. J.*, **20**(6), 747–752.
- King, S.D. & Anderson, D.L., 1998. Edge-driven convection, *Earth planet. Sci. Lett.*, **160**(3–4), 289–296.
- Kreemer, C., Blewitt, G. & Klein, E.C., 2014. A geodetic plate motion and Global Strain Rate Model, *Geochem. Geophys. Geosyst.*, **15**(10), 3849–3889.
- Kronbichler, M., Heister, T. & Bangerth, W., 2012. High accuracy mantle convection simulation through modern numerical methods, *Geophys. J. Int.*, **191**(1), 12–29.
- Laske, G., Masters, G., Ma, Z. & Pasyanos, M., 2013. Update on CRUST1.0 - A 1-degree global model of Earth's crust, in *Proceedings of the EGU General Assembly 2013*, held 7–12 April, 2013 in Vienna, Austria, id. EGU2013-2658.
- Lee, H., Kim, H., Kagoshima, T., Park, J.-O., Takahata, N. & Sano, Y., 2019. Mantle degassing along strike-slip faults in the Southeastern Korean Peninsula, *Sci. Rep.*, **9**, 15334.
- Lee, K. & Yang, W.-S., 2006. Historical seismicity of Korea, *Bull. seism. Soc. Am.*, **96**(3), 846–855.
- Lee, S.-J., Rhie, J., Kim, S., Kang, T.-S. & Kim, G.B., 2015. Ambient seismic noise tomography of the southern East Sea (Japan Sea) and the Korea Strait, *Geosci. J.*, **19**, 709–720.
- Lee, S., 2021. ASPECT parameter files for building stress field of Korea Peninsula, figshare. Dataset. doi.org/10.6084/m9.figshare.14045063.v1.
- Lee, S., Saxena, A. & Choi, E., 2020. Velocity2Temperature.V1.0.zip. Figshare. Software. doi.org/10.6084/m9.figshare.12512720.v1.
- Lithgow-Bertelloni, C. & Guynn, J.H., 2004. Origin of the lithospheric stress field, *J. geophys. Res.*, **109**(B1), B01408. doi.org/10.1029/2003JB002467.
- Mazzotti, S., 2007. Geodynamic models for earthquake studies in intraplate North America, in *Continental Intraplate Earthquakes: Science, Hazard, and Policy Issues*, Vol. **425**, pp. 17–33, eds Stein, S. & Mazzotti, S., Geological Society of America.
- McDonough, W.F. & Rudnick, R.L., 1998. Mineralogy and composition of the upper mantle, *Rev. Mineral.*, **37**, 139–164.
- Molchan, G.M. & Kagan, Y.Y., 1992. Earthquake prediction and its optimization, *J. geophys. Res.*, **97**(B4), 4823–4838.
- Mooney, W.D., Ritsema, J. & Hwang, Y.K., 2012. Crustal seismicity and the earthquake catalog maximum moment magnitude (M<sub>max</sub>) in stable continental regions (SCRs): correlation with the seismic velocity of the lithosphere, *Earth planet. Sci. Lett.*, **357**358, 78–83.
- Park, S.-I., Kwon, S., Kim, S.W., Hong, P.S. & Santosh, M., 2018. A Mesozoic orogenic cycle from post-collision to subduction in the southwestern Korean Peninsula: new structural, geochemical, and chronological evidence, *J. Asian Earth Sci.*, **157**, 166–186.
- Paul, J., Ghosh, A. & Conrad, C.P., 2019. Traction and strain-rate at the base of the lithosphere: an insight into cratonic survival, *Geophys. J. Int.*, **217**, 1024–1033.
- Priestley, K. & McKenzie, D., 2006. The thermal structure of the lithosphere from shear wave velocities, *Earth planet. Sci. Lett.*, **244**(1–2), 285–301.
- Rhie, J. & Kim, S., 2011. Regional moment tensor determination in the southern Korean Peninsula, *Geosci. J.*, **14**, 329–333.
- Rose, I., Buffett, B. & Heister, T., 2017. Stability and accuracy of free surface time integration in viscous flows, *Phys. Earth planet. Inter.*, **262**, 90–100.
- Rutter, E. & Brodie, K., 2004. Experimental intracrystalline plastic flow in hotpressed synthetic quartzite prepared from Brazilian quartz crystals, *J. Struct. Geol.*, **26**, 259–270.
- Rybacki, E. & Dresen, G., 2000. Dislocation and diffusion creep of synthetic anorthite aggregates, *J. geophys. Res.*, **105**, 26 017–26 036.
- Saxena, A., Choi, E., Powell, C.A. & Aslam, K.S., 2021. Seismicity in the central and southeastern United States due to upper mantle heterogeneities, *Geophys. J. Int.*, **225**, 1624–1636.
- Saxena, S.K., 1988. Assessment of thermal expansion, bulk modulus, and heat capacity of enstatite and forsterite, *J. Phys. Chem. Solids*, **49**(10), 1233–1235.
- Sibson, R.H., 1990. Rupture nucleation on unfavorably oriented faults, *Bull. seism. Soc. Am.*, **80**, 1580–1604.
- Sloan, R.A., Jackson, J.A., McKenzie, D. & Priestley, K., 2011. Earthquake depth distributions in central Asia, and their relations with lithospheric thickness, shortening and extension, *Geophys. J. Int.*, **185**, 1–29.
- Soh, I., Chang, C., Lee, J., Hong, T.-K. & Park, E.-S., 2018. Tectonic stress orientations and magnitudes, and friction of faults, deduced from earthquake focal mechanism inversions over the Korean Peninsula, *Geophys. J. Int.*, **213**(2), 1360–1373.
- Song, J.-H., Kim, S. & Rhie, J., 2020. Heterogeneous modification and reactivation of a craton margin beneath the Korean Peninsula from teleseismic travel time tomography, *Gondwana Res.*, **81**, 475–489.
- Soto-Cordero, L., Meltzer, A. & Stachnik, J.C., 2018. Crustal structure, intraplate seismicity, and seismic hazard in the Mid-Atlantic United States, *Seismol. Res. Lett.*, **89**(1), 241–252.
- Steinberger, B., 2016. Topography caused by mantle density variations: observation-based estimates and models derived from tomography and lithosphere thickness, *Geophys. J. Int.*, **205**, 604–621.

- Suzuki, I., 1975. Thermal expansion of periclase and olivine, and their anharmonic properties, *J. Phys. Earth*, **23**(2), 145–159.
- Tao, K., Grand, S.P. & Niu, F., 2018. Seismic structure of the upper mantle beneath Eastern Asia from full waveform seismic tomography, *Geochem. Geophys. Geosyst.*, **19**(8), 2732–2763.
- Tesuaro, M., Kaban, M.K. & Mooney, W.D., 2015. Variations of the lithospheric strength and elastic thickness in North America, *Geochem. Geophys. Geosyst.*, **16**, 2197–2220.
- Tozer, B., Sandwell, D.T., Smith, W.H.F., Olson, C., Beale, J.R. & Wessel, P., 2019. Global bathymetry and topography at 15 Arc Sec: SRTM15+, *Earth Space Sci.*, **6**, 1847–1864.
- Turcotte, D.L. & Schubert, G., 2002. *Geodynamics*. Cambridge Univ. Press.
- Vavryčuk, V., 2014. Iterative joint inversion for stress and fault orientations from focal mechanisms, *Geophys. J. Int.*, **199**, 69–77.
- Woo, J.U., Rhie, J., Kim, S., Kang, T.S., Kim, K.H. & Kim, Y., 2019. The 2016 Gyeongju earthquake sequence revisited: aftershock interactions within a complex fault system, *Geophys. J. Int.*, **217**(1), 58–74.

## SUPPORTING INFORMATION

Supplementary data are available at [GJI](#) online.

**Table S1.** Elasticity parameters of mantle minerals (table A.1 in Cammarano *et al.* 2003).

**Figure S1.** Reference geotherms for the oceanic and continental upper mantle from Turcotte & Schubert (2002), along with their average geotherms.

**Figure S2.** (a) Temperature and (b) viscosity at 35°N. Blue line in panel (b) represents the isotherm at 1300 K.

**Figure S3.** Surface transects at (a) 36°N, (b) 38°N for Case 2–1, (c) 36°N, (d) 38°N for Case 2–2, (e) 36°N and (f) 38°N for Case 2–3.

**Figure S4.** Spatial distribution of the velocity, density and viscosity for Case 2–3 at (a) the surface and (b) a depth of 100 km; along transects (c) AA along 36°N, (d) BB along 38°N, (e) CC along 125.5°E and (f) DD along 129.5°E. Red dashed lines indicate the Plate boundaries (Bird 2003). Yellow triangles in (b) indicate Cenozoic volcanism (Global Volcanism Program 2013). The blue, orange, red and dark red contours represent temperatures at 1300, 1600 and 1900 K, respectively. Yellow stars indicate epicentres that are ±1° adjacent to the transects and  $\geq M_L$  4.0. Note that the depth of the earthquakes was fixed at 20 km for visualization; the velocity fields were resampled by taking the average velocity in  $1^\circ \times 1^\circ$  bins in map view and  $1^\circ \times 30$  km for vertical transects. OT, Okinawa Trough.

**Figure S5.** Spatial distributions of the seismic moment (N·m) density across an area of  $0.4^\circ \times 0.4^\circ$ . White dots indicate the epicentres of events ( $M_L \geq 2$ ) since 1978 (KMA).

**Figure S6.** Spatial distribution of the inferred lithospheric thickness with the 1300 K isotherm for events of  $M_L \geq 4$  (magenta stars). The black-dashed lines represent the thicknesses of 97 and 139 km.

**Figure S7.** (a) Shear-wave splitting measurements and (b) epicentre of the 15 deep-focus events, as obtained from Kang & Shin (2009).

**Figure S8.** Mean angular deviations between the direction of the thickness-averaged flow in the horizontal components of cases (a) 2–1, (b) 2–2 and (c) 2–3 and the shear-wave splittings from Kang & Shin (2009). We vertically averaged the horizontal components of the velocity in increments of 20 km from a depth of 100 km. The smallest mean angular deviation is marked red in (a–c). Spatial

distribution of the thickness-averaged flow in the horizontal components with respect to the smallest mean angular deviation in cases (d) 2–1, (e) 2–2 and (f) 2–3. The orange bar represents the fast directions.

## APPENDIX A: DERIVATION OF EQUATIONS FOR ANHARMONIC EFFECTS

We closely followed the method of Cammarano *et al.* (2003) for inferring upper-mantle temperatures. The basic idea was to extrapolate density and elastic moduli based on anharmonic and anelastic parameters for various compositional models. We revisited the equations in Cammarano *et al.* (2003)'s Appendix A with respect to temperature ( $T$ ). We assumed that for a fixed pressure  $P_0$ , density at temperature  $T$  is determined with respect to the reference value at  $T_0$  (room temperature is 298.15 K) (Saxena 1988):

$$\rho(T_{\text{pot}}, P_0) = \rho(T_0, P_0) \exp\left(-\int_{T_0}^{T_{\text{pot}}} -\alpha(T) dT\right), \quad (\text{A.1})$$

where  $\alpha$  is the thermal expansion coefficient and is assumed to be in the polynomial form (Saxena 1988):

$$\alpha(T) = \alpha_0 + \alpha_1 T + \alpha_2 T^{-1} + \alpha_3 T^{-2} + \dots \quad (\text{A.2})$$

The polynomial form is one of the proposed models for the function of temperature for thermal expansion coefficients (Suzuki 1975). These coefficients have no physical meaning in  $\alpha_1$ – $\alpha_3$ . They are calculated by fitting the experimental data in a least-squares manner. Inserting the polynomial form into eq. (A.1), we obtain the following equation:

$$\begin{aligned} \rho(T_{\text{pot}}, P_0) = \rho(T_0, P_0) \exp &\left( - \left\{ \alpha_0 (T_{\text{pot}} - T_0) \right. \right. \\ &+ \frac{1}{2} \alpha_1 (T_{\text{pot}}^2 - T_0^2) + \alpha_2 (\ln(T_{\text{pot}}) - \ln(T_0)) + \dots \left. \left. \right\} \right) \end{aligned} \quad (\text{A.3})$$

After the initial density is corrected by the potential temperature, which is assumed to be 1600 K using the polynomial thermal expansion coefficients, the density is further corrected via strain based on the third-order Birch–Murnaghan equation of state (Birch 1947).

$$P + (1 + \epsilon)^{\frac{5}{2}} \left\{ 3K\epsilon + \frac{1}{2}9K(4 - K')\epsilon^2 + \dots \right\} = 0, \quad (\text{A.4})$$

where  $K$  is the bulk modulus and  $K'$  is the pressure derivative of the bulk modulus. To calculate the strain ( $\epsilon$ ), we used the assumed depth- and temperature-dependent bulk pressure of various minerals calculated using BurnMan Version 0.9.0 (Cottaar *et al.* 2014), elastic modulus, and their derivatives. After solving eq. (A.4) using the Newton–Raphson method and calculating the strain corresponding to pressure, the density for the given  $T$  and  $P$  was sequentially calculated, and is expressed as:

$$\rho(T, P) = (1 - 2\epsilon)^{\frac{3}{2}} \rho(T_{\text{pot}}, P_0) \quad (\text{A.5})$$

In addition to the absolute density at the given  $T$  and  $P$ , we calculated the derivative of density with respect to temperature ( $T$ ), using the chain rule as follows:

$$\partial\rho(T, P) = (1 - 2\epsilon)^{\frac{3}{2}} \rho(T_{\text{pot}}, P_0) \{\alpha_0 + \alpha_1(T - T_0)\} \partial T \quad (\text{A.6})$$

When the pressure was fixed, we derived the elastic moduli with respect to  $T$ :

$$\partial M(T) = \left\{ \left( \frac{\partial K}{\partial T} \right)_P + \frac{4}{3} \left( \frac{\partial G}{\partial T} \right)_P \right\} \partial T, \quad (\text{A.7})$$

where  $M$  is the  $P$  wave or the confined modulus and  $G$  is the shear modulus. Elastic moduli at a high temperature can be obtained in several ways; a common scheme is to perform a Taylor expansion (Duffy & Anderson 1989). As such, we started with the equation for  $M'$  put forth by Duffy & Anderson (1989) with the pressure derivatives of elastic moduli as follows:

$$M'(T) = M'(T_0) \exp \left( \int_{T_0}^T \alpha(T) dT \right) \quad (\text{A.8})$$

We further derived eq. (A.8) with respect to temperature, using the chain rule as follows:

$$\partial M'(T) = M'(T_0) \exp \left( \int_{T_0}^T \alpha(T) dT \right) \alpha(T) \partial T. \quad (\text{A.9})$$

The moduli at the given  $T$  and  $P$  conditions (Duffy & Anderson 1989; Cammarano *et al.* 2003) with the truncated second order of  $\epsilon$  are as follows:

$$K + \frac{4}{3}G = (1 - \epsilon)^{\frac{5}{2}} \left( K + \frac{4}{3}G + \epsilon \left( 5 \left( K + \frac{4}{3}G \right) - 3K \left( K' + \frac{4}{3}G' \right) \right) \right). \quad (\text{A.10})$$

We further derived eq. (A.10) with respect to temperature, using the chain rule as follows:

$$\begin{aligned} \partial M = (1 - 2\epsilon)^{\frac{5}{2}} & \left[ \frac{\partial M(T)}{\partial T} \partial T + \epsilon \left\{ 5 \frac{\partial M(T)}{\partial T} \partial T - 3 \frac{\partial K(T)}{\partial T} \right. \right. \\ & \times \left( \frac{\partial K}{\partial P} - \left( \frac{4}{3} \right) \frac{\partial G}{\partial P} \right) \partial T - 3K(T) \partial M'(T) \left. \right] \end{aligned} \quad (\text{A.11})$$

Velocity is defined by the square root of the elastic modulus over density, and the independent variables are the functions of temperature, pressure and chemical components. Thus, the partial derivatives can be expressed as follows:

$$\partial V = \partial \left( \sqrt{\frac{M(T, P, C)}{\rho(T, P, C)}} \right) = \frac{1}{2\sqrt{\rho M}} \partial M - \frac{\sqrt{M}}{2\rho^{\frac{3}{2}}} \partial \rho. \quad (\text{A.12})$$

By inserting eq. (A.6) into  $\rho$  in eq. (A.12) and eq. (A.11) into  $M$  in eq. (A.12), we can calculate the  $P$ -wave velocity derivatives due to the anharmonic effect. When  $K + 4G/3$  is replaced with  $G$ , the  $S$ -wave velocity derivatives due to the anharmonic effect are complementary.

## APPENDIX B: SUPPLEMENTARY MATERIAL

In this section, readers can find the details regarding numerical modelling (e.g. input parameters, reference geotherms); some of the results overlap with those presented in Sections 3 and 4 of the main text.